Geochemical and isotopic signatures of magmatic products in the MAR rift valley at 12°49'–17°23' N and 29°59'–33°41' N: Evidence of Two contrasting sources of the parental melts

S.A. Silantyev, L.V. Danyushevsky, A.A. Plechova, Laure Dosso, B.A. Bazylev, V.E. Bel'Tenev

Geochemical and Isotopic Signatures of Magmatic Products in the MAR Rift Valley at 12°49′–17°23′ N and 29°59′–33°41′ N: Evidence of Two Contrasting Sources of the Parental Melts

S. A. Silantyev[a], L. V. Danyushevsky[b], A. A. Plechova[a], L. Dosso[c], B. A. Bazylev[a], and V. E. Bel'tenev[d]

[a] *Vernadsky Institute of Geochemistry and Analytical Chemistry, Russian Academy of Sciences, ul. Kosygina 19, Moscow, 119991 Russia*

e-mail: silantyev@geokhi.ru

[b] *University of Tasmania, GPO Box 252-79, TAS 7001, Hobart, Australia*

[c] *Institute Français de Recherche pour L'exploration de la Mer, BP 70-29280 Plouzane Cedex, Brest, France*

[d] *Polar Geological Exploration Expedition, ul. Pobedy 24, Lomonosov, 189510 Russia*

Abstract—Data presented in the paper suggest significant differences between the thermodynamic conditions under which magmatic complexes were formed in MAR at 29°–34° N and 12°–18° N. The melts occurring at 29°–34° N were derived by the melting of a mantle source with a homogeneous distribution of volatile components and arrived at the surface without significant fractionation, likely, due to their rapid ascent. The MAR segments between 12° and 18° N combine contrasting geodynamic environments of magmatism, which predetermined the development of a large plume region with the widespread mixing of the melting products of geochemically distinct mantle sources. At the same time, this region is characterized by conditions favorable for the origin of localized zones of anomalous plume magmatism. These sporadic magmatic sources were spatially restricted to MAR fragments with the Hess crust, whose compositional and mechanical properties were, perhaps, favorable for the focusing and localization of plume magmatism. The plume source between 12° and 18° N beneath MAR may be geochemically heterogeneous.

INTRODUCTION

Our research was principally centered on the comparative analysis of newly obtained geochemical and isotopic data on the composition of basalts from the MAR rift valley, collected at two geodynamically significant segments of its axial zone: 12°49′–17°23′ N and 29°59′–33°41′ N (Fig. 1). The former of them includes a sharp-gradient geochemical anomaly at 14°48′ N and is located in the junction zone of the 15°20′ transform fault zone and two segments of contrasting magmatism: northern normal and southern anomalous (Bougault et al., 1988; Dosso et al., 1991; Sobolev et al., 1992; Silantyev et al., 1998). The other segment is spatially restricted to the southern periphery of the Azores plume province and includes an intersection area of the MAR axial zone and the Hayes transform, with this area currently regarded as the boundary between the anomalous northern MAR segment (Azores megaplume) and its southern segment, which is characterized by normal spreading magmatism (Smith et al., 1998; Bideau et al., 1998). Thus, both regions show obvious evidence of petrologic–geochemical segmentation in the basaltic layer of the MAR axial zone, which determines the importance of these segments for the identification of the geochemical nature of mantle reservoirs related to the rift-valley magmatism and for the elucidation of the interaction character of the geochemically contrasting melts. Obviously, the newly obtained data may provide a basis for assaying the specifics of the magmatic products characteristic of normal (spreading) and anomalous (plume) MAR segments and for revealing possible differences in the fluid regime of magmatism related to the geochemical types of the sources. Our research is topical and urgent because:

(1) This publication reports our recently obtained data on the geochemical characteristics of magmatic products from segments of the MAR rift valley north and south of the geochemical anomaly at 14°48′ N, the largest and highest gradient anomaly in the Atlantic, and makes it possible to revise the scale of this anomaly and its spatial structure. A still uncertain issue is the northern and southern boundaries of this anomaly. Indeed, the composition of magmatic products in the rift valley segments farther south and north of the 15°20′ transform fault zone is still poorly known, and there are no corresponding data on the MAR segment north of 17° N. The MAR segments between 12°49′ and 17°23′ N is now thought (see, for example, Xia

Fig. 1. Surface topography of the axial MAR zone according to (*Relief...*, 1991).

Ellipses mark the sampling areas of chilled glasses. Numerals denote hydrothermal fields and occurrences of ore mineralization within MAR: (1) Ashadze, (2) Logachev, (3) 16°38′, (4) Snake Pit, (5) TAG, (6) Broken Spur, (7) Lost City, (8) Rainbow, (9) Lucky Strike, (10) Menez Gwen.

et al., 1992; Cannat and Casey, 1995; Casey et al., 1995) to be characterized by a low magmatic budget and the absence of correspondence between the actual structure of the crustal section and the thickness of the basaltic layer estimated by petrological and geochemical methods. At the same time, recent deep-sea drilling data obtained during Leg 209 of the drillship *Joides Resolution* (*Shipboard...*, 2003) provide convincing evidence that this MAR segment includes areas in which residual peridotites are exposed that are the most depleted among all currently known to occur in the world system of mid-oceanic ridges (see, for example,

Silantyev, 2003). The newly obtained data on the geochemistry of basalts from the unexplored MAR segments between 12°49′ and 17°23′ N provide for the resolution of the inconsistency implied by the close spatial association of extremely depleted peridotites and enriched basalts in this region.

(2) The areas where the MAR axial zone intersects the Atlantis, Petrov and Hayes transform fault zones (29°59′–33°41′ N) are still poorly examined in terms of the isotopic–geochemical parameters of their basalts. Because of this, all new data on these areas are of principal importance for reproducing the shortwavelength compositional segmentation in the southern periphery of the Azores superplume.

Our rock collection consisted of 71 samples of predominantly glassy pillow basalts recovered from 38 dredging sites; 40 glassy chilled crusts were analyzed for major and trace elements, including volatiles, and Sr, Nd, and Pb isotopic composition was determined for 21 samples.

Twenty samples of our collection were taken in the MAR axial zone between 17° and 17°23′ N, in the ridge segment at the northern termination of the 14°48′ geochemical anomaly. Until now any data on the composition of magmatic products from this MAR segment were lacking. Our collection included 12 samples from the rift valley segment between 12°49′ and 12°57′ N, whose geochemistry is still also studied very poorly. At the same time, any information of the rock compositions in this segment of the MAR rift valley is of paramount importance in light of the recent discovery of an extensive hydrothermal field (Ashadze field) at 12°58′ N during a cruise of the R/V *Professor Logachev.*

METHODS

Concentrations of major elements, Cl and S were analyzed on Cameca SX50 and SX100 microprobes at the University of Tasmania in Hobart at an accelerating voltage of 15 kV and a beam current of 20 nA (beam diameter 5 μm). The analyses were conducted with the use of the USNM 111240/2 standard (VG2 basaltic glass), which was provided for this research by courtesy of Dr. Jarosewich (Jarosewich et al., 1980). Major elements were determined accurate to 2%. The detection limits for Cl ad S were 22 and 150 ppm, respectively, and they were analyzed accurate to >30 and 50%, respectively.

Trace elements were analyzed by ICP-MS with laser ablation (LA-ICP-MS mass spectrometry) at the University of Tasmania. The analyses were carried out using a new UP213 Nd-YAF (213 nm) laser coupled with an Agilent 4500 Quadrupled mass spectrometer. The analyses were conduced in a He atmosphere at spots ~100 μm in diameter, with a 10 Hz laser repetition rate and a laser energy density of ~12 J/cm^{-2}. The counting time of individual analyses was 90 s and included 30 s for background measurements (in switched-off laser mode) and 60 s for measurements at a switched-on laser. The analytical setup was calibrated using the NIST612 glass standard. All measured values were normalized to the USGS BCR-2g standard glass. Each of the analyses listed in Table 3 is an average of two individual spot analyses spaced ~200 μm apart.

The H_2O concentrations in the glasses were determined by infrared spectrometry (FTIR) on a Brucker IFS 66 spectrometer equipped with an optical microscope. Doubly polished glass platelets 50–250 μm thick and 2–5 mm in diameter were analyzed at 3–6 spots. The diameter of the analytical spots was 60 μm, which precluded the occurrence of microlites in the analyzed volume. We did not detect any differences greater than the analytical precision (2–3%) between the H_2O concentrations obtained in three replicate analyses of the glasses at the same spots.

In all instances (except isotopic analyses), the measurements were conducted within the same areas (~1 mm in diameter) in chilled glass fragments. The samples were first analyzed for H_2O and then on an electron microprobe and by LA-ICP-MS. To test the compositional homogeneity of the analyzed fragments of the chilled glasses, we analyzed them in two discrete areas in eight samples (Tables 2 and 3). The results do not display compositional variations greater than the analytical accuracy, and this led us to regard our data as reliable.

The Sr and Nd isotopic composition of the chilled glasses was measured on a Finnigan MAT-261 7-collector mass spectrometer at IFREMER, Brest, France, by conventional techniques adopted at this research center (Dosso et al., 1999).

MATERIALS

This research was conduced using glass samples from the chilled crusts of pillow basalts dredged during cruise 16 of the R/V *Akademik Boris Petrov* and cruises 19 and 20 of the R/V *Professor Logachev* (Table 1). According to the sampling sites, our collection can be grouped as follows: (1) MAR between 12°49′ and 17°23′ N—axial high (35%), eastern wall of the rift valley (16%), and western wall of the rift valley (49%); and (2) MAR between 29°59′ and 33°41′ N—axial high (25%), eastern wall of the rift valley (5%), western wall of the rift valley (20%), and the intersection zone of the transform and rift valley (50%). The rocks associated with chilled glasses are dominated by basalts, and peridotites and amphibolites were dredged only from the western wall of the rift valley at 12°57′ N (Table 1).

The representative collection of rock samples examined in the course of this research most comprehensively characterizes the mineralogical and textural diversity of the petrographic types of basalts from the rift valley of the MAR segment in question. Below we give a concise petrographic description of the samples.

Table 1. MAR segments from which chilled glass and basalt samples were dredged

Sample no.	R/V, cruise	Rock	Latitude, N	Longitude, W	Depth, m	Area	Related rocks
L20-719-1	*Logachev*, 20	Basalt	17.3	46.53	3380–3087	WW RV	Only basalts
L20-719-3	*Logachev*, 20	Basalt	17.3	46.53	3380–3087	WW RV	Only basalts
L20-719-5	*Logachev*, 20	Glass	17.3	46.53	3380–3087	WW RV	Only basalts
L20-724-1	*Logachev*, 20	Basalt	17.26	46.49	3862–3581	WW RV	Only basalts
L20-724-5	*Logachev*, 20	Basalt + glass	17.26	46.49	3862–3581	WW RV	Only basalts
L20-724-6	*Logachev*, 20	Basalt + glass	17.26	46.49	3862–3581	WW RV	Only basalts
L20-729-2	*Logachev*, 20	Basalt + glass	17.22	46.55	3518–3316	WW RV	Only basalts
L20-733-1	*Logachev*, 20	Basalt	17.18	46.52	3910–3780	AH RV	Only basalts
L20-733-12	*Logachev*, 20	Basalt + glass	17.18	46.52	3910–3780	AH RV	Only basalts
L20-733-13b	*Logachev*, 20	Basalt + glass	17.18	46.52	3910–3780	AH RV	Only basalts
L20-733-13a	*Logachev*, 20	Basalt + glass	17.18	46.52	3910–3780	AH RV	Only glass
L20-736-15	*Logachev*, 20	Glass	17.38	46.47	3640–3274	WW RV	Only basalts
L20-737-6	*Logachev*, 20	Glass	17.38	46.53	3150–2905	WW RV	Only basalts
L20-738-1	*Logachev*, 20	Basalt	17.26	46.45	3880	AH RV	Only basalts
L20-738-2	*Logachev*, 20	Glass	17.26	46.45	3880	AH RV	Only basalts
L20-741-3	*Logachev*, 20	Glass	17.2	46.52	3920–3670	WW RV	Only basalts
L20-743-2	*Logachev*, 20	Basalt + glass	17.18	46.56	3392–3195	WW RV	Only basalts
L20-743-9	*Logachev*, 20	Glass	17.18	46.56	3392–3195	WW RV	Only basalts
L20-744-1	*Logachev*, 20	Basalt + glass	17.15	46.48	3960–3590	AH RV	Only basalts
L20-744-9	*Logachev*, 20	Glass	17.15	46.48	3960–3590	AH RV	Only basalts
L20-773-3	*Logachev*, 20	Basalt	16.83	46.5	3900–3640	WW RV	Peridotites
L20-773-6	*Logachev*, 20	Doleritic basalt	16.84	46.5	3900–3640	WW RV	Peridotites
L20-775-4	*Logachev*, 20	Glass	16.84	46.5	3910–3700	WW RV	Peridotites
L20-776-4	*Logachev*, 20	Basalt + glass	16.95	46.54	3390–3225	WW RV	Peridotites
L20-792-1	*Logachev*, 20	Basalt	16.12	46.62	3160–3023	AH RV	Only basalts
L20-792-3	*Logachev*, 20	Glass	16.12	46.62	3160–3023	AH RV	Only basalts
L20-793-2	*Logachev*, 20	Basalt + glass	16.13	46.62	3210–3010	AH RV	Only basalts
L20-794-1	*Logachev*, 20	Basalt + glass	16.15	46.62	3294–3010	AH RV	Only basalts
L20-794-2	*Logachev*, 20	Glass	16.15	46.62	3294–3010	AH RV	Only basalts
L20-794-9/GL	*Logachev*, 20	Glass	16.15	46.62	3294–3010	AH RV	Only basalts
L20-796-3	*Logachev*, 20	Glass	16.14	46.63	3060–3065	AH RV	Only basalts
L20-801-5	*Logachev*, 20	Glass	16.17	46.53	2908–2765	EW RV	Only basalts
L20-804-2	*Logachev*, 20	Basalt + glass	16.13	46.54	3140–2966	EW RV	Only basalts
L20-805-1	*Logachev*, 20	Basalt + glass	16.12	46.52	3030–2835	EW RV	Only basalts
L20-806-3	*Logachev*, 20	Glass	16.14	46.58	3531–3355	AH RV	Only basalts
L20-806-3	*Logachev*, 20	Glass	16.14	46.58	3531–3355	AH RV	Only basalts
L20-807-4	*Logachev*, 20	Basalt + glass	16.18	46.62	3342–3171	AH RV	Only basalts
L20-811-1	*Logachev*, 20	Basalt + glass	16.1	46.54	3154–2893	EW RV	Only basalts

Table 1. (Contd.)

Sample no.	R/V, cruise	Rock	Latitude, N	Longitude, W	Depth, m	Area	Related rocks
L20-811-2	*Logachev*, 20	Basalt + glass	16.1	46.54	3154–2893	EW RV	Only basalts
L20-827-2-3	*Logachev*, 20	Glass	12.92	44.88	4077	WW RV	Only basalts
L20-841-5	*Logachev*, 20	Doleritic basalt	13.02	44.92	3220–2685	WW RV	Pyroxenites
L20-852-15	*Logachev*, 20	Glass	12.91	44.89	4050	WW RV	Only basalts
L20-853-3	*Logachev*, 20	Basalt + glass	12.92	44.9	2827	WW RV	Only basalts
L20-860-2	*Logachev*, 20	Basalt	12.82	44.77	2428–1940	EW RV	Only basalts
L20-860-7	*Logachev*, 20	Glass	12.82	44.77	2428–1940	EW RV	Only basalts
L20-871-2	*Logachev*, 20	Basalt + glass	12.93	44.94	3360–3330	WW RV	Only basalts
L20-892-19	*Logachev*, 20	Basalt + glass	12.95	44.93	3660–3340	WW RV	Peridotites, amphibolites; and metabasalts
L20-892-20	*Logachev*, 20	Basalt	12.95	44.93	3660–3340	WW RV	Peridotites, amphibolites; and metabasalts
L20-897-5	*Logachev*, 20	Glass	12.89	44.79	3502	EW RV	Only basalts
L20-900-2	*Logachev*, 20	Basalt	12.94	44.89	4066	WW RV	Only basalts
L20-912-4	*Logachev*, 20	Glass	12.83	44.98	3053–2894	WW RV	Only basalts
16ABP-24-6	*ABP*, 16	Basalt	33.53	38.99	2550–2250	EW RV	Only basalts
16ABP-7-9A/AR1	*ABP*, 16	Basalt + glass	30.58	41.88	3470–3319	AH RV	Only basalts
16ABP-7-9A/AR2	*ABP*, 16	Basalt + glass	30.58	41.88	3470–3319	AH RV	Only basalts
16ABP-7-3	*ABP*, 16	Basalt + glass	30.58	41.88	3470–3319	AH RV	Only basalts
16ABP-10	*ABP*, 16	Basalt + glass	31.35	41.13	3340–3139	AH RV	Only basalts
16ABP-35-7	*ABP*, 16	Basalt	30.8	41.75	3389–3200	AH RV	Only basalts
16ABP-45-77/AR1	*ABP*, 16	Basalt + glass	29.99	42.65	3145–2706	WIRT MAR-Atlantis	Only basalts
16ABP-45-77/AR2	*ABP*, 16	Basalt + glass	29.99	42.65	3145–2706	WIRT MAR-Atlantis	Only basalts
16ABP-5-8/AR1	*ABP*, 16	Basalt + glass	31.1	41.42	3400–3279	WIR MAR-Petrov	Only basalts
16ABP-5-8/AR2	*ABP*, 16	Basalt + glass	31.1	41.42	3400–3279	WIR MAR-Petrov	Only basalts
16ABP-6/AR1	*ABP*, 16	Basalt + glass	30.4	41.94	3250–2990	WIR MAR-Petrov	Only basalts
16ABP-6/AR2	*ABP*, 16	Basalt + glass	30.4	41.94	3250–2990	WIR MAR-Petrov	Only basalts
16ABP-6-4/AR1	*ABP*, 16	Basalt + glass	30.4	41.94	3250–2990	WIR MAR-Petrov	Only basalts
16ABP-6-4/AR2	*ABP*, 16	Basalt + glass	30.4	41.94	3250–2990	WIR MAR-Petrov	Only basalts
16ABP-6-42/AR1	*ABP*, 16	Basalt + glass	30.4	41.94	3250–2990	WIR MAR-Petrov	Only basalts
16ABP-6-42/AR2	*ABP*, 16	Basalt + glass	30.4	41.94	3250–2990	WIR MAR-Petrov	Only basalts
19L-610-3	*Logachev*, 19	Basalt + glass	16.73	46.62	3259–2821	WW RV	Only basalts
16ABP-65-1/AR1	*ABP*, 16	Basalt + glass	15.03	44.94	3699–3518	WW RV	Only basalts
16ABP-65-1/AR2	*ABP*, 16	Basalt + glass	15.03	44.94	3699–3518	WW RV	Only basalts
16ABP-65-27	*ABP*, 16	Basalt + glass	15.03	44.94	3699–3518	WW RV	Only basalts

Note: Angular minutes are represented as decimal fractions of angular degrees. WW RV and EW RV are the western and eastern walls of the rift valley, AH RV is the axial high of the rift valley, WIR MAR-Petrov is the western intersection of MAR with the Petrov transform fault, WIR MAR-Atlantis is the western intersection of MAR with the Atlantis transform fault, *Logachev* is the R/V *Logachev*, *ABP* is the R/V *Akademik Boris Petrov*.

Table 2. Concentration (wt %) of major components and volatiles in glasses and chilled crusts of pillow basalts

Component	29°59′–33°41′ N													16°44′–17°23′ N	
	16ABP-24-6*	16ABP-5-8	16ABP-5-8	16ABP-7-9A	16ABP-7-9A	16ABP-6	16ABP-6	16ABP-6-4	16ABP-6-4	16ABP-6-42	16ABP-6-42	16ABP-45-77	16ABP-45-77	L20-736-15	L20-736-15
		a**	b	a	b	a	b	a	b	a	b	a	b	1	2
SiO_2	50.63	50.68	50.73	50.59	50.63	50.52	50.59	50.83	50.87	51.03	50.85	49.89	49.78	51.04	50.89
TiO_2	1.90	1.69	1.69	1.31	1.33	1.33	1.31	1.26	1.27	1.26	1.25	1.60	1.63	1.38	1.39
Al_2O_3	14.10	14.67	14.83	15.53	15.54	15.37	15.44	15.16	15.15	15.21	15.18	15.49	15.65	16.01	15.98
FeO*	12.45	11.01	11.03	9.93	9.94	9.90	9.89	10.02	9.97	10.06	9.95	10.73	10.70	9.44	9.46
MnO	0.22	0.19	0.20	0.18	0.21	0.18	0.18	0.19	0.19	0.18	0.21	0.20	0.19	0.17	0.18
MgO	6.18	7.69	7.58	7.75	7.69	7.82	7.87	7.79	7.81	7.84	7.83	7.76	7.79	7.88	7.88
CaO	10.49	10.81	10.94	11.61	11.55	11.99	12.00	11.89	11.92	11.92	11.85	10.70	10.73	11.64	11.75
Na_2O	2.87	2.67	2.60	2.49	2.49	2.54	2.53	2.37	2.42	2.43	2.42	2.94	2.93	2.87	2.87
K_2O	0.113	0.084	0.083	0.075	0.073	0.048	0.050	0.055	0.052	0.054	0.058	0.093	0.092	0.078	0.079
P_2O_5	0.172	0.161	0.163	0.116	0.114	0.104	0.099	0.108	0.098	0.092	0.094	0.136	0.141	0.117	0.109
Cr_2O_3	0.013	0.048	0.050	0.056	0.057	0.056	0.059	0.040	0.034	0.038	0.042	0.038	0.048	0.045	0.047
S	0.158	0.142	0.137	0.126	0.132	0.130	0.134	0.127	0.134	0.133	0.137	0.128	0.132	0.112	0.118
Cl	0.0056	0.0029	0.0033	0.0039	0.0044	<0.0022	0.0025	0.0022	<0.0022	0.0023	<0.0022	0.0048	0.0036	0.0060	0.0048
H_2O	0.344	0.274	0.270	0.223	0.225	0.163	0.159	0.167	0.159	0.173	0.161	0.316	0.303	0.160	0.160
Total	99.65	100.13	100.32	99.99	99.98	100.15	100.32	100.01	100.09	100.42	100.03	100.01	100.12	100.94	100.91

Component	16°44′–17°23′ N														
	L20-736-15	L20-737-6	L20-737-6	L20-719-5	L20-719-5	L20-724-5	L20-724-5	L20-724-6	L20-738-2	L20-738-2	L20-729-2	L20-741-3	L20-733-12	L20-733-13	L20-743-9
	3	1	2	1	2	1	2		1	2					1
SiO_2	50.99	51.42	51.11	51.99	51.51	49.54	49.15	49.61	51.33	51.19	51.08	51.35	50.84	50.82	51.48
TiO_2	1.41	1.42	1.44	1.53	1.50	1.13	1.13	1.16	1.67	1.71	1.47	1.61	1.98	2.03	1.19
Al_2O_3	15.97	15.73	15.65	15.01	14.97	16.69	16.60	16.72	15.62	15.43	15.67	15.24	15.15	15.11	15.75
FeO*	9.46	9.87	9.82	10.34	10.22	11.43	11.57	11.50	10.38	10.35	9.77	10.38	11.49	11.51	8.94
MnO	0.16	0.19	0.21	0.18	0.16	0.21	0.19	0.19	0.21	0.20	0.19	0.19	0.18	0.21	0.17
MgO	7.92	7.83	7.84	7.29	7.20	8.20	8.43	8.13	7.43	7.43	8.02	7.38	7.08	7.11	8.02
CaO	11.86	11.38	11.40	11.89	11.78	10.76	10.58	10.88	11.01	11.17	11.66	11.45	10.38	10.59	12.16
Na_2O	2.85	2.83	2.81	2.84	2.86	2.82	2.73	2.79	2.96	2.95	2.73	2.84	2.96	3.03	2.85
K_2O	0.076	0.071	0.067	0.091	0.092	0.040	0.043	0.047	0.102	0.104	0.091	0.086	0.193	0.187	0.088
P_2O_5	0.124	0.122	0.120	0.112	0.117	0.075	0.083	0.072	0.161	0.141	0.131	0.126	0.202	0.185	0.101
Cr_2O_3	0.053	0.045	0.062	0.043	0.053	0.035	0.040	0.045	0.044	0.044	0.054	0.045	0.051	0.038	0.062
S	0.123	0.140	0.128	0.141	0.137	0.131	0.133	0.138	0.133	0.140	0.131	0.143	0.144	0.140	0.117
Cl	0.0043	0.0061	0.0047	0.0060	0.0066	0.0051	0.0044	0.0059	0.0054	0.0041	0.0057	0.006	0.010	0.0097	0.0055
H_2O	0.154	0.160	0.156	0.180	0.183	0.119	0.109	0.116	0.207	0.205	0.162	0.184	0.293	0.295	0.139
Total	101.15	101.23	100.81	101.64	100.79	101.18	100.79	101.39	101.28	101.08	101.17	101.02	100.96	101.26	101.07

Table 2. (Contd.)

Component	16°44′–17°23′ N								16°7′–16°10′ N						
	L20-743-9	L20-744-1	L20-744-1	L20-744-9	L20-776-4	L20-776-4	L20-775-4	19L-610-3	L20-801-5	L20-801-5	L20-794-1	L20-794-2	L20-796-3	L20-806-3	L20-793-2
	2	**1**	**2**		**1**	**2**			**1**	**2**					
SiO_2	51.44	48.37	48.34	48.79	51.29	51.34	50.47	49.46	51.71	51.51	51.31	51.15	51.60	51.97	51.89
TiO_2	1.19	0.85	0.85	0.83	1.35	1.37	1.22	1.03	1.46	1.43	1.45	1.45	1.50	1.31	1.38
Al_2O_3	15.90	17.79	17.87	17.91	15.90	15.84	15.67	16.19	15.32	15.26	16.30	16.26	15.31	15.86	15.59
FeO*	8.89	10.87	10.78	10.91	9.50	9.19	9.00	10.28	9.96	9.88	8.75	8.69	9.59	8.98	9.11
MnO	0.18	0.17	0.19	0.19	0.19	0.19	0.14	0.20	0.17	0.18	0.16	0.15	0.17	0.17	0.16
MgO	7.96	8.72	8.73	8.92	7.86	8.01	9.46	8.88	7.99	7.90	8.05	8.07	7.95	8.02	8.06
CaO	12.00	11.31	11.22	11.31	11.63	11.66	11.69	11.30	11.25	11.14	11.62	11.51	11.06	11.50	11.50
Na_2O	2.86	2.39	2.48	2.49	2.80	2.69	2.41	2.42	2.69	2.64	2.87	2.72	2.66	2.67	2.72
K_2O	0.096	0.021	0.027	0.020	0.091	0.175	0.118	0.063	0.188	0.184	0.448	0.439	0.237	0.240	0.223
P_2O_5	0.094	0.048	0.044	0.055	0.100	0.123	0.114	0.071	0.150	0.145	0.219	0.224	0.153	0.145	0.161
Cr_2O_3	0.060	0.037	0.042	0.027	0.060	0.065	0.069	0.041	0.052	0.051	0.045	0.042	0.053	0.060	0.040
S	0.116	0.124	0.121	0.134	0.123	0.120	0.121	0.114	0.113	0.111	0.103	0.107	0.121	0.109	0.118
Cl	0.0062	0.0037	0.0048	0.0031	0.005	0.0124	0.0070	0.003	0.012	0.010	0.014	0.0156	0.012	0.013	0.012
H_2O	0.138	0.065	0.062	0.059	0.169	0.225	0.155	0.139	0.244	0.259	0.276	0.272	0.252	0.270	0.233
Total	100.94	100.78	100.76	101.64	101.06	101.01	100.65	100.19	101.31	100.70	101.61	101.10	100.67	101.31	101.19

Component	16°7′–16°10′ N			15°1.8′ N			12°49′–12°57′ N								
	L20-792-3	L20-805-1	L20-805-1	16ABP-65-1	16ABP-65-1	16ABP-65-27	L20-892-19	L20-871-2	L20-853-3	L20-852-15	L20-897-5	L20-912-4	L20-860-7	L20-860-7	L20-860-7
		1	**2**	*a*	*b*								**1**	**2a**	**2b**
SiO_2	52.01	50.73	50.71	51.08	51.07	52.09	51.57	50.48	50.88	51.31	51.30	51.53	51.59	51.55	51.64
TiO_2	1.20	1.57	1.55	1.06	1.08	1.32	1.73	1.48	1.80	1.47	1.52	1.49	1.41	1.48	1.49
Al_2O_3	15.46	16.20	16.23	15.51	15.66	16.25	14.80	15.77	14.73	15.61	15.25	15.10	15.31	15.50	15.56
FeO*	8.55	10.13	10.28	9.01	8.82	9.31	10.69	10.78	11.45	10.05	10.01	10.14	9.72	10.09	10.06
MnO	0.15	0.16	0.16	0.17	0.17	0.18	0.19	0.20	0.19	0.20	0.17	0.17	0.18	0.17	0.18
MgO	8.16	7.24	7.30	8.31	8.26	7.68	6.79	7.76	7.24	7.88	7.84	7.82	7.69	7.61	7.46
CaO	12.49	10.81	10.76	11.90	11.79	11.57	11.01	11.27	10.47	11.57	11.24	11.45	11.41	11.37	11.38
Na_2O	2.39	3.12	3.16	2.16	2.20	2.00	2.72	2.42	2.62	2.49	2.50	2.51	2.50	2.53	2.54
K_2O	0.184	0.389	0.396	0.298	0.299	0.453	0.289	0.194	0.294	0.255	0.326	0.223	0.221	0.223	0.225
P_2O_5	0.127	0.265	0.281	0.129	0.133	0.180	0.203	0.152	0.229	0.170	0.189	0.180	0.147	0.173	0.151
Cr_2O_3	0.060	0.036	0.034	0.047	0.049	0.059	0.044	0.057	0.024	0.046	0.034	0.034	0.044	0.035	0.055
S	0.112	0.130	0.130	0.112	0.109	0.121	0.137	0.117	0.149	0.124	0.134	0.122	0.113	0.136	0.125
Cl	0.0092	0.024	0.024	0.012	0.013	0.023	0.013	0.013	0.013	0.016	0.014	0.011	0.012	0.016	0.018
H_2O	0.178	0.329	0.330	0.461	0.458	0.532	0.325	0.254	0.354	0.277	0.316	0.270	0.261	0.303	0.303
Total	101.09	101.14	101.33	100.26	100.11	101.76	100.49	100.95	100.45	101.47	100.84	101.05	100.61	101.19	101.19

Note: All Fe is given in the form of FeO, * Here and in Table 3—sample number. ** Here and in Table 3 in this line, **1**, **2**, and **3** are three separate glass fragments of the same sample, and **a** and **b** are two discrete areas within the same glass fragment.

Table 3. Concentrations (ppm) of trace elements in the basaltic glasses

Element	29°59′–33°41′ N												
	16ABP-24-6	16ABP-5-8	16ABP-5-8	16ABP-7-9A	16ABP-7-9A	16ABP-6	16ABP-6	16ABP-6-4	16ABP-6-4	16ABP-6-42	16ABP-6-42	16ABP-45-77	16ABP-45-77
		a	**b**	**a**	**b**	**a**	**b**	**a**	**b**	**a**	**b**	**a**	**b**
Li	8.24	6.83	6.99	5.93	5.83	6.04	6.09	5.91	5.92	6.08	5.98	6.48	6.48
Be	0.596	0.497	0.439	0.393	0.405	0.352	0.343	0.323	0.335	0.288	0.362	0.530	0.592
Sc	45.1	39.6	39.7	41.3	40.7	42.0	42.2	42.1	42.2	41.9	42.1	40.6	39.1
Co	47.2	46.5	47.1	46.1	46.2	45.6	45.5	47.4	47.0	47.7	46.8	46.7	45.7
Ni	48.5	116.3	117.6	115.6	117.1	96.3	94.3	89.8	91.0	92.2	90.7	134.3	133.0
Cu	64.2	67.4	67.3	85.6	86.7	82.2	81.4	83.9	84.7	85.0	84.8	86.4	82.1
Zn	105	85	84	72	73	75	72	73	74	79	80	82	75
Rb	2.22	0.77	0.78	0.83	0.79	0.44	0.44	0.53	0.55	0.57	0.55	1.16	1.15
Ba	20.2	8.5	8.6	9.7	9.5	5.1	5.2	6.5	6.6	6.6	6.5	10.9	11.1
U	0.076	0.044	0.039	0.045	0.041	0.028	0.028	0.033	0.032	0.035	0.033	0.051	0.047
Th	0.251	0.124	0.120	0.122	0.123	0.080	0.072	0.082	0.084	0.088	0.099	0.152	0.134
Nb	3.32	1.85	1.85	1.80	1.79	1.05	1.07	1.27	1.29	1.30	1.28	2.74	2.70
Ta	0.232	0.139	0.130	0.127	0.125	0.080	0.082	0.090	0.093	0.096	0.092	0.198	0.184
La	4.04	3.22	3.17	2.58	2.59	2.09	2.10	2.10	2.11	2.11	2.14	3.45	3.37
Ce	13.0	11.1	11.1	8.6	8.5	7.3	7.4	7.1	7.2	7.3	7.2	11.2	11.1
Pb	0.530	0.401	0.415	0.404	0.350	0.330	0.329	0.285	0.296	0.278	0.289	0.478	0.421
Sr	100	106	106	101	101	92	93	90	91	92	92	120	121
Nd	13.18	11.107	10.897	8.1552	8.0458	7.9573	8.096	7.2283	7.3566	7.4557	7.6132	10.589	10.478
Zr	129	105	104	78	77	74	76	67	68	67	69	108	104
Hf	3.73	2.98	2.91	2.18	2.11	2.24	2.20	1.96	1.98	1.97	2.07	2.84	2.81
Sm	4.91	3.87	3.86	3.15	3.04	3.17	3.19	2.84	2.88	2.87	2.90	3.87	3.70
Ti	11716	9912	10081	8266	8278	8148	8159	7848	7811	7868	7812	9789	9669
Eu	1.65	1.40	1.40	1.15	1.12	1.16	1.17	1.05	1.07	1.10	1.11	1.38	1.34
Gd	7.11	5.45	5.33	4.47	4.26	4.57	4.68	4.14	4.24	4.22	4.26	5.31	5.11
Dy	8.49	6.71	6.56	5.39	5.19	5.51	5.58	5.09	5.08	5.22	5.22	6.34	6.18
Er	5.29	4.33	4.16	3.35	3.29	3.45	3.51	3.23	3.29	3.31	3.35	4.06	4.00
Y	46.0	36.9	36.2	29.3	28.7	30.4	30.8	28.1	28.6	28.4	29.1	35.3	34.3
Yb	5.16	3.92	3.92	3.24	3.14	3.41	3.37	3.10	3.21	3.17	3.30	3.81	3.66
Lu	0.79	0.59	0.57	0.49	0.47	0.49	0.50	0.47	0.47	0.47	0.49	0.59	0.53
$(La/Sm)_{cn}$	0.53	0.54	0.53	0.53	0.55	0.43	0.42	0.48	0.47	0.48	0.48	0.58	0.59

Table 3. (Contd.)

Element	16°44′–17°23′ N												
	L20-736-15	L20-736-15	L20-736-15	L20-737-6	L20-737-6	L20-719-5	L20-719-5	L20-724-5	L20-724-5	L20-724-6	L20-738-2	L20-738-2	L20-729-2
	1	**2**	**3**	**1**	**2**	**2**	**2**	**1**	**2**		**1**	**2**	
Li	6.10	6.13	6.30	6.34	6.38	6.75	6.75	4.69	4.55	4.74	6.96	7.15	6.76
Be	0.420	0.439	0.437	0.445	0.444	0.460	0.460	0.298	0.282	0.335	0.550	0.571	0.479
Sc	37.0	37.0	37.3	37.2	37.8	41.7	41.7	34.6	33.5	35.0	38.2	38.0	37.1
Co	42.7	42.7	43.6	43.6	45.3	42.4	42.4	53.5	53.6	52.8	42.0	43.0	45.1
Ni	100.1	99.3	102.9	108.7	112.8	67.8	67.8	167.2	169.5	149.6	96.0	99.3	115.2
Cu	72.5	71.5	73.4	69.4	73.8	78.9	78.9	95.5	97.6	94.6	62.6	65.1	71.1
Zn	66	67	67	70	71	74	74	82	78	86	74	79	75
Rb	0.74	0.76	0.77	0.71	0.73	1.00	1.00	0.51	0.51	0.55	0.98	1.01	0.97
Ba	9.4	9.2	9.4	8.7	8.5	12.8	12.8	7.5	7.0	7.4	11.9	11.7	11.5
U	0.042	0.043	0.041	0.039	0.036	0.050	0.050	0.027	0.026	0.029	0.058	0.061	0.043
Th	0.110	0.109	0.121	0.102	0.104	0.149	0.149	0.074	0.070	0.077	0.163	0.160	0.144
Nb	1.80	1.86	1.88	1.69	1.65	2.29	2.29	1.22	1.19	1.23	2.50	2.53	2.26
Ta	0.134	0.128	0.133	0.114	0.112	0.149	0.149	0.081	0.079	0.081	0.182	0.174	0.149
La	2.73	2.71	2.74	2.65	2.63	3.06	3.06	1.65	1.53	1.64	3.63	3.60	2.96
Ce	9.3	9.2	9.3	9.3	9.2	10.3	10.3	5.7	5.3	5.7	12.0	12.3	10.2
Pb	0.469	0.352	0.417	0.445	0.391	0.478	0.478	0.284	0.258	0.249	0.549	0.568	0.398
Sr	113	115	116	102	100	109	109	115	110	117	114	116	113
Nd	9.445	9.0746	9.2624	9.4111	9.2131	10.136	10.136	6.203	5.6859	6.233	11.883	11.925	9.6382
Zr	84	86	86	86	86	90	90	51	49	53	112	112	90
Hf	2.46	2.38	2.42	2.49	2.37	2.65	2.65	1.64	1.46	1.63	3.23	3.16	2.50
Sm	3.32	3.21	3.39	3.39	3.48	3.63	3.63	2.40	2.32	2.45	4.26	4.20	3.41
Ti	8389	8489	8561	8660	8644	9314	9314	7013	6691	7136	10289	10499	9082
Eu	1.26	1.21	1.25	1.26	1.25	1.34	1.34	1.01	0.92	0.99	1.50	1.51	1.23
Gd	4.69	4.67	4.68	4.67	4.61	5.20	5.20	3.68	3.41	3.80	5.90	5.68	4.82
Dy	5.48	5.36	5.48	5.62	5.46	6.10	6.10	4.65	4.19	4.77	6.83	6.70	5.84
Er	3.38	3.35	3.42	3.41	3.43	3.75	3.75	2.97	2.71	3.03	4.23	4.15	3.45
Y	29.7	30.3	30.3	31.2	30.9	33.1	33.1	25.7	24.2	26.5	37.3	37.2	31.3
Yb	3.26	3.31	3.35	3.41	3.28	3.73	3.73	2.98	2.67	3.16	4.09	4.06	3.38
Lu	0.49	0.48	0.48	0.48	0.50	0.53	0.53	0.43	0.42	0.44	0.63	0.59	0.49
$(La/Sm)_{cn}$	0.53	0.55	0.52	0.51	0.49	0.55	0.55	0.44	0.43	0.43	0.55	0.55	0.56

Table 3. (Contd.)

Element	16°44′–17°23′ N											
	L20-741-3	L20-733-12	L20-733-13	L20-743-9	L20-743-9	L20-744-1	L20-744-1	L20-744-9	L20-776-4	L20-776-4	L20-775-4	19L-610-3
				1	**2**	**1**	**2**		**1**	**2**		
Li	6.99	8.20	8.55	5.76	5.49	3.96	3.89	3.90	6.02	5.90	5.50	5.59
Be	0.525	0.630	0.625	0.388	0.392	0.208	0.202	0.206	0.431	0.512	0.435	0.262
Sc	39.4	36.1	36.7	38.0	37.7	35.0	34.5	34.9	35.7	35.8	35.3	42.2
Co	42.5	44.7	45.6	42.1	42.2	55.0	55.2	53.9	42.8	42.1	47.2	51.4
Ni	85.7	107.3	109.9	82.0	82.1	188.3	188.6	180.6	113.8	128.0	208.3	152.9
Cu	69.2	57.0	55.6	83.9	82.9	105.5	110.8	101.4	73.8	76.4	81.6	84.9
Zn	77	90	91	61	60	70	68	69	67	67	63	69
Rb	0.91	3.04	3.13	1.10	1.03	0.19	0.19	0.17	1.19	2.95	1.53	0.92
Ba	11.3	34.1	36.8	13.7	13.9	2.8	2.8	3.0	15.7	38.1	21.4	11.0
U	0.051	0.127	0.132	0.050	0.043	0.010	0.011	0.013	0.052	0.112	0.068	0.037
Th	0.137	0.396	0.415	0.130	0.145	0.033	0.033	0.036	0.147	0.345	0.206	0.121
Nb	2.16	5.88	5.99	2.24	2.23	0.52	0.53	0.53	2.49	5.16	3.11	1.88
Ta	0.158	0.386	0.397	0.150	0.153	0.034	0.038	0.034	0.169	0.342	0.210	0.126
La	3.17	5.50	5.72	2.51	2.57	1.00	0.96	0.98	2.87	4.46	3.45	1.94
Ce	10.7	16.2	17.0	8.2	8.2	3.7	3.6	3.7	9.1	12.4	10.3	6.0
Pb	0.516	0.701	0.611	0.346	0.458	0.229	0.178	0.217	0.391	0.479	0.407	0.258
Sr	105	108	110	119	120	101	99	101	124	133	117	74
Nd	10.608	14.111	14.816	7.7373	7.8728	4.2671	4.1244	4.3354	8.7529	10.199	9.1299	5.9523
Zr	97	127	129	70	69	35	34	34	79	88	81	55
Hf	2.85	3.58	3.81	1.96	2.00	1.06	0.99	1.14	2.23	2.38	2.23	1.61
Sm	3.80	4.80	5.00	2.77	2.75	1.71	1.71	1.68	3.14	3.48	3.13	2.44
Ti	9803	11989	12338	7404	7269	5186	5023	5218	8230	8419	7630	6376
Eu	1.42	1.69	1.77	1.11	1.11	0.76	0.74	0.77	1.19	1.25	1.12	0.93
Gd	5.42	6.60	6.83	3.90	3.95	2.84	2.64	2.77	4.31	4.51	4.22	3.74
Dy	6.31	7.60	7.82	4.67	4.63	3.85	3.68	3.80	5.04	5.17	4.82	5.00
Er	3.97	4.65	4.83	2.93	2.94	2.68	2.51	2.67	3.12	3.18	3.08	3.42
Y	34.9	41.5	42.2	25.6	25.5	22.7	22.0	22.3	28.1	28.0	27.1	29.3
Yb	3.76	4.59	4.75	2.79	2.83	2.80	2.61	2.79	3.05	3.08	3.02	3.56
Lu	0.58	0.67	0.70	0.40	0.41	0.41	0.40	0.41	0.45	0.44	0.42	0.54
$(La/Sm)_{cn}$	0.54	0.74	0.74	0.59	0.60	0.38	0.36	0.38	0.59	0.83	0.71	0.51

Table 3. (Contd.)

Element	16°07′–16°10′ N										15°1.8′ N		
	L20-801-5	L20-801-5	L20-794-1	L20-794-2	L20-796-3	L20-806-3	L20-793-2	L20-792-3	L20-805-1	L20-805-1	16ABP-65-1	16ABP-65-1	16ABP-65-27
	1	**2**							**1**	**2**	**a**	**b**	
Li	6.34	6.19	5.18	5.19	6.29	5.39	5.22	5.86	5.58	5.52	4.52	4.62	5.13
Be	0.518	0.495	0.670	0.688	0.537	0.517	0.459	0.493	0.809	0.754	0.485	0.520	0.764
Sc	35.9	36.4	32.9	32.4	35.8	36.5	36.0	36.0	28.4	28.3	38.6	38.1	36.1
Co	44.5	43.2	41.5	41.5	42.7	41.4	41.3	42.4	43.1	43.2	43.8	44.9	45.4
Ni	126.5	122.9	126.1	131.4	127.3	126.8	121.1	118.3	114.7	114.5	119.7	130.8	122.9
Cu	81.4	80.9	73.4	72.5	70.2	82.7	81.3	75.6	67.8	67.6	84.3	86.2	90.3
Zn	74	72	64	64	70	63	62	67	84	81	62	62	77
Rb	3.54	3.42	6.99	6.95	4.12	4.04	2.86	3.67	7.16	7.12	5.52	5.69	8.89
Ba	46.1	44.4	126.6	124.2	52.4	56.8	41.7	49.7	125.0	126.1	76.4	76.0	108.9
U	0.137	0.131	0.255	0.254	0.163	0.157	0.104	0.138	0.378	0.394	0.181	0.187	0.288
Th	0.429	0.425	0.813	0.793	0.483	0.525	0.319	0.433	1.177	1.191	0.681	0.675	1.036
Nb	6.40	6.44	11.96	11.80	7.39	7.58	5.84	6.63	13.71	13.74	9.61	9.57	14.50
Ta	0.404	0.405	0.754	0.748	0.458	0.503	0.372	0.411	0.826	0.824	0.634	0.630	0.912
La	5.21	5.03	8.96	8.86	5.74	5.81	4.15	5.14	11.93	11.90	6.99	6.94	9.63
Ce	14.0	13.5	20.7	20.4	15.2	14.6	11.0	13.6	26.6	26.6	16.0	16.0	22.6
Pb	0.495	0.466	0.727	0.646	0.521	0.584	0.342	0.527	0.889	0.876	0.564	0.541	0.711
Sr	126	124	253	251	134	153	156	136	342	340	157	155	193
Nd	10.72	10.413	12.794	12.493	11.579	10.757	8.1949	10.365	15.425	15.545	9.934	9.8318	13.17
Zr	86	88	98	98	97	86	65	87	99	99	73	72	96
Hf	2.48	2.43	2.60	2.55	2.74	2.42	1.76	2.36	2.64	2.65	1.90	1.83	2.42
Sm	3.51	3.52	3.53	3.52	3.77	3.34	2.64	3.32	4.00	4.01	2.73	2.70	3.39
Ti	8869	8736	8989	8863	9094	8231	7349	8532	9389	9408	6711	6706	8416
Eu	1.31	1.27	1.31	1.29	1.35	1.24	1.02	1.23	1.50	1.51	0.96	0.97	1.13
Gd	4.60	4.65	4.17	4.15	4.90	4.22	3.45	4.44	4.71	4.70	3.27	3.15	4.02
Dy	5.32	5.30	4.49	4.36	5.54	4.77	3.75	4.94	4.57	4.65	3.45	3.42	3.91
Er	3.22	3.26	2.64	2.56	3.41	2.86	2.27	2.97	2.52	2.55	2.07	2.00	2.37
Y	28.5	29.0	23.4	23.3	29.8	25.4	20.6	26.8	23.1	23.1	18.5	17.9	20.8
Yb	3.14	3.17	2.41	2.43	3.28	2.78	2.24	2.94	2.27	2.44	1.95	1.94	2.27
Lu	0.46	0.45	0.36	0.34	0.47	0.39	0.31	0.42	0.33	0.35	0.29	0.29	0.36
$(La/Sm)_{cn}$	0.96	0.92	1.64	1.63	0.98	1.13	1.02	1.00	1.93	1.92	1.65	1.66	1.84

Table 3. (Contd.)

Element	12°49′–12°57′ N								2σ error (%)	BCR-2
	L20-892-19	L20-871-2	L20-853-3	L20-852-15	L20-897-5	L20-912-4	L20-860-7	L20-860-72		
							1	**2b**		
Li	6.73	5.98	7.23	5.73	6.02	6.20	6.10	6.26	4.0	9.2
Be	0.638	0.568	0.722	0.568	0.618	0.576	0.605	0.617	11.8	2.3
Sc	39.3	37.3	37.5	38.7	36.4	39.0	39.1	38.0	3.9	32.6
Co	41.6	46.6	45.7	44.1	44.0	44.3	45.2	45.8	4.1	39
Ni	67.8	142.0	100.4	115.7	113.0	103.6	101.7	118.9	4.5	12.1
Cu	68.5	89.0	62.7	77.7	63.6	65.3	72.4	73.1	4.5	19
Zn	78	79	85	70	71	73	80	82	4.5	125
Rb	4.98	2.49	5.22	4.63	6.17	3.97	4.08	4.04	5.5	46.8
Ba	56.6	31.1	62.5	59.4	76.6	48.6	47.1	48.3	4.9	682
U	0.191	0.128	0.206	0.176	0.212	0.161	0.149	0.146	11.6	1.7
Th	0.614	0.374	0.652	0.604	0.713	0.500	0.516	0.506	7.6	6.05
Nb	9.47	5.61	9.71	8.73	11.03	7.39	7.21	6.88	4.6	12
Ta	0.600	0.373	0.624	0.573	0.677	0.456	0.490	0.456	7.5	0.81
La	6.86	4.84	7.54	6.50	7.61	5.84	5.68	5.91	4.3	25
Ce	17.6	13.2	19.7	16.3	18.8	15.2	14.6	15.5	4.1	53.7
Pb	0.578	0.496	0.813	0.570	0.588	0.516	0.560	0.557	7.5	10
Sr	134	118	127	139	152	131	125	131	4.0	333
Nd	12.636	10.528	14.407	11.361	12.267	11.016	11.282	11.213	4.6	28.6
Zr	112	94	122	96	104	97	98	96	4.0	183
Hf	2.98	2.69	3.26	2.71	2.71	2.58	2.81	2.76	5.1	4.9
Sm	3.94	3.49	4.45	3.45	3.62	3.49	3.22	3.40	5.9	6.6
Ti	10666	9137	10811	8906	9398	9284	8927	9089	5.4	13434
Eu	1.37	1.26	1.57	1.26	1.26	1.25	1.22	1.28	5.4	1.95
Gd	5.23	4.94	5.83	4.57	4.60	4.76	4.75	4.65	5.4	6.68
Dy	5.85	5.70	6.50	5.10	5.04	5.29	5.17	5.45	4.6	6.3
Er	3.53	3.53	4.00	3.19	3.06	3.31	3.26	3.30	4.8	3.61
Y	32.4	31.0	36.1	27.7	27.6	29.4	29.1	29.5	3.9	33.4
Yb	3.56	3.52	4.00	3.16	2.94	3.23	3.16	3.27	5.5	3.38
Lu	0.51	0.52	0.58	0.46	0.43	0.46	0.48	0.48	5.7	0.5
$(La/Sm)_{cn}$	1.13	0.90	1.09	1.22	1.36	1.08	1.14	1.12		

Note: Average accuracy of the measurements 2σ; $(La/Sm)_{cn}$ ratio is the La/Sm ratio normalized to C1 chondrite (Sun and McDonough, 1989).

MAR between 29°59′ and 33°41′ N

Axial high. The predominant type of basalts in the axial zone of this MAR segment is olivine- and plagioclase-phyric pillow basalts with usually weakly altered chilled glass. The varieties of these rocks rich in olivine phenocrysts occasionally contain, along with olivine and plagioclase, also clinopyroxene. The phase proportions significantly vary from sample to sample. Sample 16ABP-7-9 consists of fresh olivine- and plagioclase-phiric pillow basalt. Its matrix consists of acicular plagioclase laths (up to 0.1 mm, 10%), rounded subhedral olivine crystals (up to 0.1 mm, <1%), clinopyroxene (<1%), and weakly altered glass (>80%). Sample 16ABP-10 is olivine- and plagioclase-phyric basalt, which is fine-grained and has a groundmass of porphyritic or microlitic texture. Olivine and plagioclase phenocrysts account for 5–6% of the rock by volume. Olivine (0.2–0.6 mm) and plagioclase (0.8–1.6 mm) phenocrysts occur as euhedral or subhedral, often resorbed crystals. The groundmass has a microlitic texture and is made up of dark brown weakly altered glass with small plagioclase laths and pores no larger than 0.1 mm. Sample 16ABP-35-7 is olivine-phyric pillow basalt, which contains, together with olivine, single phenocrysts of clinopyroxene and plagioclase. The groundmass consists of olivine, clinopyroxene, plagioclase, and glass. The cores of the pillows contain 60–70 vol % chilled glass.

Eastern wall of the rift valley. Scarce samples collected in this area represent mostly plagioclase-phyric varieties of clinopyroxene-, olivine- and plagioclase-phyric pillow basalts (for example, sample 16ABP-24-6). The crystallinity of the matrix of these rocks varies from vitrophyric to microlitic. In the latter case, the weakly altered glass abounds in acicular plagioclase microlites.

Intersection with the Atlantis transform fault zone. The area is dominated by plagioclase-phyric pillow basalts (for example, sample 16ABP-45-77). The plagioclase (10–25%) contains round or angular inclusions of weakly altered glass. The texture of the matrix is microlitic, grading in places into hyalopilitic. The matrix contains plagioclase and olivine microlites.

Intersection with the Petrov transform fault zone (between the Atlantis and Hayes transforms). The samples collected in the area commonly represent fresh, glassy, highly porous pillow basalts (for example, samples 16ABP-5-8 and 16ABP-6), which may be either aphyric or plagioclase-phyric. The groundmass consists of olivine (<1%), plagioclase (up to 10%), clinopyroxene (<1%), and glass (80–90%) and has a variolitic texture.

MAR between 12°49′ and 17°23′ N, North of the 15°20′ Transform Fault

Axial high. The predominant rock type in this area is fresh plagioclase- or olivine-phyric vitreous pillow basalts. Sample 738-1 is plagioclase-phyric highly porous basalt, whose groundmass consists of fresh glass with tiny plagioclase needles. Sample 744-1 is vitreous basalt with rare olivine phenocrysts and a subintersertal matrix of brown glass with plagioclase microlites. Sample 807-4 is aphyric hyalobasalt with an intersertal texture and a matrix of fresh glass with minute olivine, plagioclase, and clinopyroxene crystals. Sample 794-1 is olivine-phyric hyalobasalt with fresh glass. The groundmass glass contains acicular plagioclase microlites. Sample 792-1 is plagioclase-phyric basalt. Its matrix of brown weakly altered glass includes large phenocrysts and laths of prismatic plagioclase.

Eastern wall of the rift valley. In the eastern wall of this MAR segment, the predominant rocks are olivine-phyric hyalobasalts. Sample 801-5 is variolitic porous hyalobasalt with very rare olivine phenocrysts and fresh glass. Sample 804-2 is olivine- and plagioclase-phyric hyalobasalt with a subintersertal texture and a groundmass with minute plagioclase needles. Sample 805-1 is olivine-phyric porous basalt with a variolitic matrix. Sample 811-1 is olivine-phyric porous hyalobasalt with fresh glass.

Western wall of the rift valley. The samples collected in this area are dominated by the following varieties of pillow basalts. Sample 719-1 is variolitic basalt with weakly altered glass and rare plagioclase and olivine phenocrysts. Sample 719-3 is an olivine-phyric porous variolitic basalt. Sample 792-2 is aphyric variolitic hyalobasalt with very rare large partly melted plagioclase phenocrysts. Sample 741-3 is olivine- and plagioclase-phyric basalt with a vitreous mesostasis with submerged acicular plagioclase laths and euhedral olivine crystals. The texture of this rock is intersertal, and its glass is fresh. Sample 733-1 is porous variolitic hyalobasalt with rare plagioclase needles. Sample 743-2 is porous aphyric hyalobasalt with a subintersertal texture. The matrix of the rock is dominated by plagioclase. Sample 773-6 is aphyric recrystallized basalt with very rare small olivine phenocrysts. Along with olivine and plagioclase, the matrix contains clinopyroxene. Sample 773-3 is olivine-phyric hyalobasalt whose matrix contains corroded olivine crystals and whose glass is weakly altered.

MAR between 12°49′ and 17°23′ N, South of the 15°20′ Transform Fault

Eastern wall of the rift valley. The relatively sparse samples collected at the eastern wall of the rift valley of this MAR segment are dominated by highly porous var-

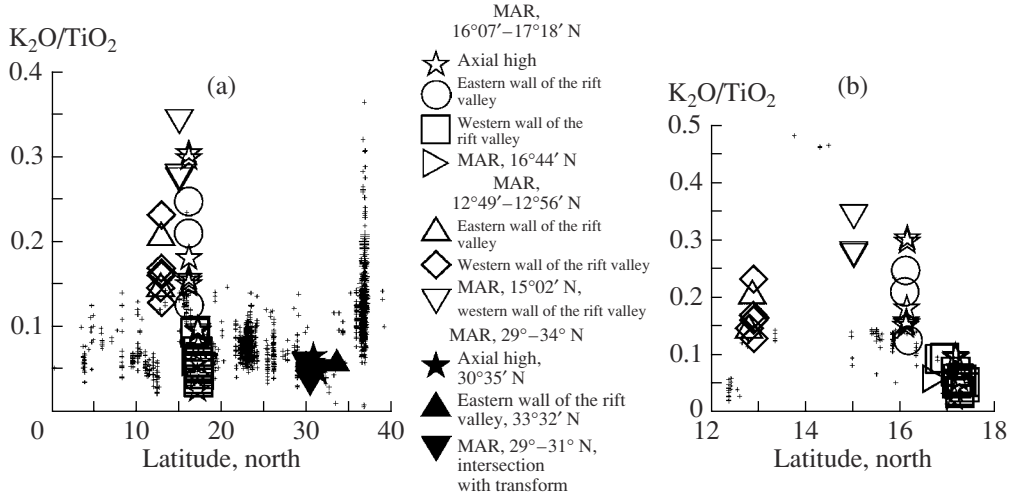

Fig. 2. Distribution of the K_2O/TiO_2 ratio in chilled glasses along the MAR axis in MAR segments between (a) 12°49′ and 17°23′ and between 29°59′ and 33°41′ N and (b) between 12°49′–17°23′ N. Small crosses correspond to glass compositions from the catalogues (*RIDGE…*, 1999; *Smithsonian…*, 2000).

iolitic basalts with sheaves of acicular plagioclase crystals (for example, in sample 860-2).

Western wall of the rift valley. The western wall of the rift valley south of the 15°20′ transform fault is dominated by the following types of basaltoids. Samples 16ABP-65-1 and 16ABP-65-27 are porous aphyric pillow basalts with chilled crusts. Sample 841-5 is plagioclase–clinopyroxene dolerite with a microblastic texture and weak traces of amphibolization. Sample 892-19 is weakly porous olivine- and plagioclase-phyric hyalobasalt. Its matrix likely contains, along with olivine and plagioclase, clinopyroxene. The groundmass texture of the rock is subintersertal. Sample 892-20 is plagioclase-, olivine-, and clinopyroxene-phyric hyalobasalt with an intersertal texture. Its matrix contains acicular plagioclase laths. Sample 900-2 is porous plagioclase-phyric basalt with rare minute olivine phenocrysts. Its intersertal matrix consists mostly of brown glass and plagioclase. Sample 827-2/3 is plagioclase- and olivine-phyric hyalobasalt with a subintersertal texture.

As can be seen from Table 1, our samples from both of the MAR segments are dominated by chilled glasses (57 samples), whereas aphyric and subporhyritic varieties of recrystsallized basalts are represented by a relatively insignificant number of samples in our collection (14 samples).

It should be emphasized that 20 samples of the collection were taken from the MAR segment north of 17° N. Data on the composition of basalts from the rift valley in this region were lacking as of yet. Equally significant 12 samples were collected at the rift valley segment between 12°49′ and 13°01′ N, including the hydrothermal field recently discovered at 13° N (Ashadze field), to which a large occurrence of base-metal sulfide ore mineralization can be related.

GEOCHEMISTRY

Major Elements

In terms of major-element composition, our chilled glasses characterize the whole MORB spectrum in the MAR axial zone (Table 2, Fig. 2a). According to the currently adopted classifications (Wilson, 1989; Sun and McDonough, 1989), the variations in the K_2O/TiO_2 ratio (0.12–0.35) of these rocks testify to the predominance of P-MORB (plume type) in the MAR segments between 12°49′ and 17°23′ N. In contrast to this area, the region between 29°59′ and 33°41′ N contains exclusively N-MORB (normal or spreading type). Newly obtained data shown in Fig. 2a are consistent with modern concepts of the longwavelength geochemical segmentation of the MAR axial zone in the northern hemisphere (see, for example, Schilling et al., 1983; Dmitriev et al., 1990; Bougault et al., 1988; Dosso et al., 1991, 1999). At the same time, the MAR segment north of the 15°20′ transform fault was determined to include a sharply localized geochemical anomaly at 16°06′–16°10′ N (Fig. 2b), which has not been known previously. Recently obtained results testify to the small-scale heterogeneity in the distribution of the K_2O/TiO_2 ratio in these segments of the MAR rift valley. In the segment immediately south of the 15°20′ transform fault, the most enriched glasses ($K_2O/TiO_2 = 0.35$) were found in the inner corner high area in the western wall of the rift valley. Farther southward, the rift valley segment between 12°49′ and 12°56′ N was determined to contain rocks with lower $K_2O/TiO_2 = 0.15–0.25$, with a symmetric distribution across the strike of the ridge axis. In the northern MAR segment, the maximum K_2O/TiO_2 values (0.30) were found in glasses from the axial high of the rift valley and its eastern wall (0.25) near 16°00′–16°01′. Much lower values of the

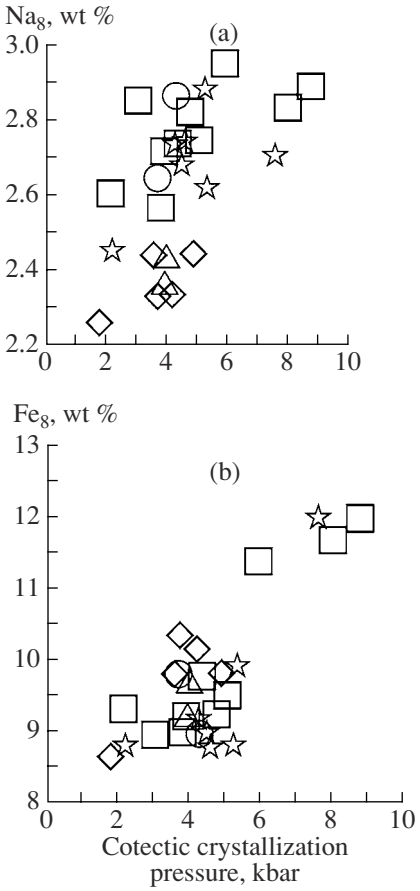

Fig. 3. Dependence of (a) the Na_8 and (b) Fe_8 parameters of the chilled glasses from MAR segments adjacent to the 15°02′ transform fault zone on the cotectic crystallization pressure of basaltic melt (estimated according Danyushevsky et al., 1996). See Fig. 2 for symbol explanations.

K_2O/TiO_2 ratio (0.03–0.10) were detected in glasses from the axial high and the western wall of the rift valley near 17° N.

It is commonly thought that the whole length of MAR along its strike in the northern hemisphere is characterized by alternating segments with a thick basaltic layer (these are usually areas of plume magmatism) and segments whose basaltic layer is reduced and whose oceanic crust belongs to the Hess type (see, for example, Klein and Langmuir, 1987; Bougault et al., 1988; Dosso et al., 1991; Gracia et al., 1998; Silantyev et al., 2001). The geochemical indicators of the thickness of the basaltic layer of the oceanic crust and petrogenetic conditions in mid-oceanic ridges most often applied in petrological practice are the Na_8 and Fe_8 concentrations in basaltic glasses (recalculated to MgO = 8 wt % in the rock). The former of these parameters makes it possible, according to (Klein and Langmuir, 1987), to evaluate the degree of melting and corresponding thickness of the basaltic crust (Na_8 decreases with increasing degrees of melting). The latter parameter allows one to assay the depth from which MORB were derived (Fe_8 increases with increasing pressure). Inasmuch as most of the glass compositions considered in this publication correspond to a narrow range of MgO concentrations (6.5–9.5 wt %), we used the Na_2O concentrations of the rocks as an indicator parameter of the degrees of melting and the thickness of the basaltic layer. The character of Na_2O distribution in chilled glasses from the two regions and the Na_8 values of glasses from the rift valley segments between 12°49′ and 17°23′ N led us to conclude that the MAR segment between 29° and 34° N is characterized by a degree of melting of the source comparable to the analogous values for the plume MAR region between 12° and 17° N. However, the sharply localized zones of plume magmatism at 15°02′ and 16°07′ N show the lowest degrees of melting. Judging from the Na_2O concentrations in the chilled glasses, the maximum degrees of melting in the two MAR segments corresponded to the inner corner high and the western wall of the rift valley near the 15°20′ transform fault. This idea finds support in estimates of the degree of melting obtained for the Cr# of spinel from mantle residues that are associated with basalts in this area and which are, judging from the data in (Silantyev, 2003), the most depleted spinel harzburgites of the Mid-Atlantic Ridge. It is also important to stress that, in spite of the aforementioned consistency of the estimated degrees of melting of the associated basaltic glasses and mantle residues, this MAR segment displays apparent inconsistency between the actual crustal stratigraphy and the thickness of the basaltic layer determined by geochemical techniques. Basaltic magmatism in this area is reduced, and the mantle residues are a strongly dominating type of the basement rocks. It also follows from the data of Table 2 that the MAR segment south of the 15°20′ transform fault is characterized by generally higher degrees of melting than degrees of melting in the northern MAR segment.

The comparison of the Na_8 parameter in our chilled glasses and the cotectic crystallization pressure of basaltic melt estimated for the same samples by the method proposed in (Danyushevsky et al., 1996) led us to suggest that the most enriched basaltic glasses collected at MAR between 12° and 17° N correspond to the lowest cotectic crystallization pressures (Fig. 3a). Obviously, these chilled glasses were produced by melts ascending to the surface from shallow magmatic sources. The depths at which the basaltic melts were generated and which were estimated for the chilled glasses from the Fe_8 values are in good agreement with the pressure estimates for cotectic crystallization calculated according to (Danyushevsky et al., 1996) (Fig. 3b).

The variations in the N_2O, Na_8, and Fe_8 values in our chilled glasses suggest that basaltic magmatism between 12° and 17° N and between 29° and 34° N at MAR is characterized by various degrees of melting

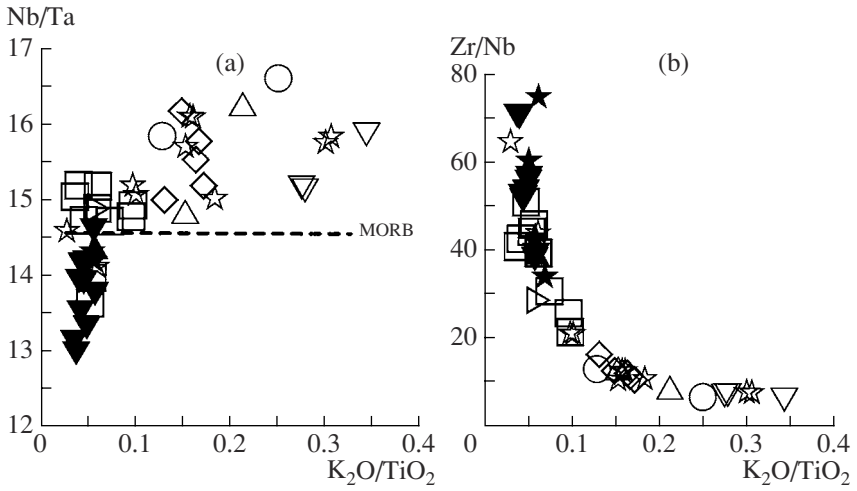

Fig. 4. Variations in (a) the K_2O/TiO_2–Nb/Ta and (b) K_2O/TiO_2–Zr/Nb ratios in the chilled glasses. The average Nb/Ta ratio for MORB is according to (Büchl et al., 2002). See Fig. 2 for symbol explanations.

and various depths of the mantle magmatic sources beneath the axial zone.

REE and Other Trace Elements

The concentration levels of highly incompatible elements is an efficient geochemical tool for distinguishing between the products of basaltic magmatism of the plume and spreading types. In this context, highly incompatible elements are particularly useful, because they are not significantly fractionated in the process of partial melting. It is usually believed that the elements conventionally used in geochemical discriminant diagrams can be arranged in the form of the following succession according to their increasing incompatibility: Hf, Zr, Ta, and Nb (Niu and Batiza, 1997). The comparison of the K_2O/TiO_2 ratio with Nb/Ta, Zr/Hf, and Zr/Nb in our samples of chilled glasses led us to the following conclusions important for interpreting the geochemical types of the magmatic products and their mantle sources in the two MAR segments. Evidently, the two major compositional groups of our chilled glasses (normal and plume) are characterized by different distribution types of incompatible elements (Fig. 4). The glasses corresponding to the N-MORB family (29°–34° N at MAR) display a narrow range of K_2O/TiO_2 variations at a significant scatter of Nb/Ta (Fig. 3a), Zr/Nb (Fig. 3b), and Zr/Hf, which suggests that they may have been formed with the participation of a compositionally similar melt that separated, however, from a mantle source with a heterogeneous distribution of incompatible elements (Table 3). At the same time, the compositional points of the chilled glasses of the P-MORB type (12°–17° N at MAR) define systematic trends in the diagrams, suggesting that the glasses may have been formed via the mixing of compositionally different parental melts, with the most enriched glasses found at 15°02′ N and 16°07′ N. It is worth mentioning that, judging from the data presented above, chilled glasses from the axial high and the western wall of the rift valley at 17°09′–17°18′ N compositionally correspond to N-MORB and are geochemically close to glasses from 29°–34° N at MAR (Fig. 2). These relations are also confirmed by the variations in the K_2O/TiO_2 and Ce/Pb ratios in our samples of chilled glasses, which, in turn, point to the possible heterogeneous Ce and Pb distributions in the mantle reservoirs beneath these MAR segments. The REE patterns of samples in our collection are consistent with the data presented above for the concentrations of major and trace elements in these samples. In the MAR segments between the Atlantis and Hayes transforms (29°–34° N), the $(La/Sm)_{cn}$ ratios in glasses from the axial high, eastern wall of the rift valley, and its intersection zones with the Atlantis, Petrov, and Hayes transform faults vary from 0.42 to 0.56. Chilled glasses from various segments of the MAR rift valley between 12° and 17° N are characterized by the following $(La/Sm)_{cn}$ ratios: (1) in the area at 17° N: 0.40–0.74 for the axial high and 0.44–0.59 for the western wall of the valley; (2) in the area at 16°44′–16°50′ N: 0.51–0.72 for the western wall of the valley; (3) in the area of the sharply localized anomaly at 16°07′ N: 1–1.63 for the axial high and 0.94–1.92 for the eastern wall of the valley; (4) in the corner high area at 15°02′ N: 1.65–1.84 for the western wall of the valley; (5) in the area of 12.82°–12.92° N: 0.90–1.36. Relations between the $(La/Sm)_{cn}$ and K_2O/TiO_2 ratios are illustrated in Fig. 5b. The values of the $(La/Sm)_{cn}$ ratio of our glasses is correlated with Zr/Hf and Zr/Nb in the same manner as with K_2O/TiO_2. Figure 5a clearly illustrates the contrasting character of the distribution of LREE concentrations in chilled

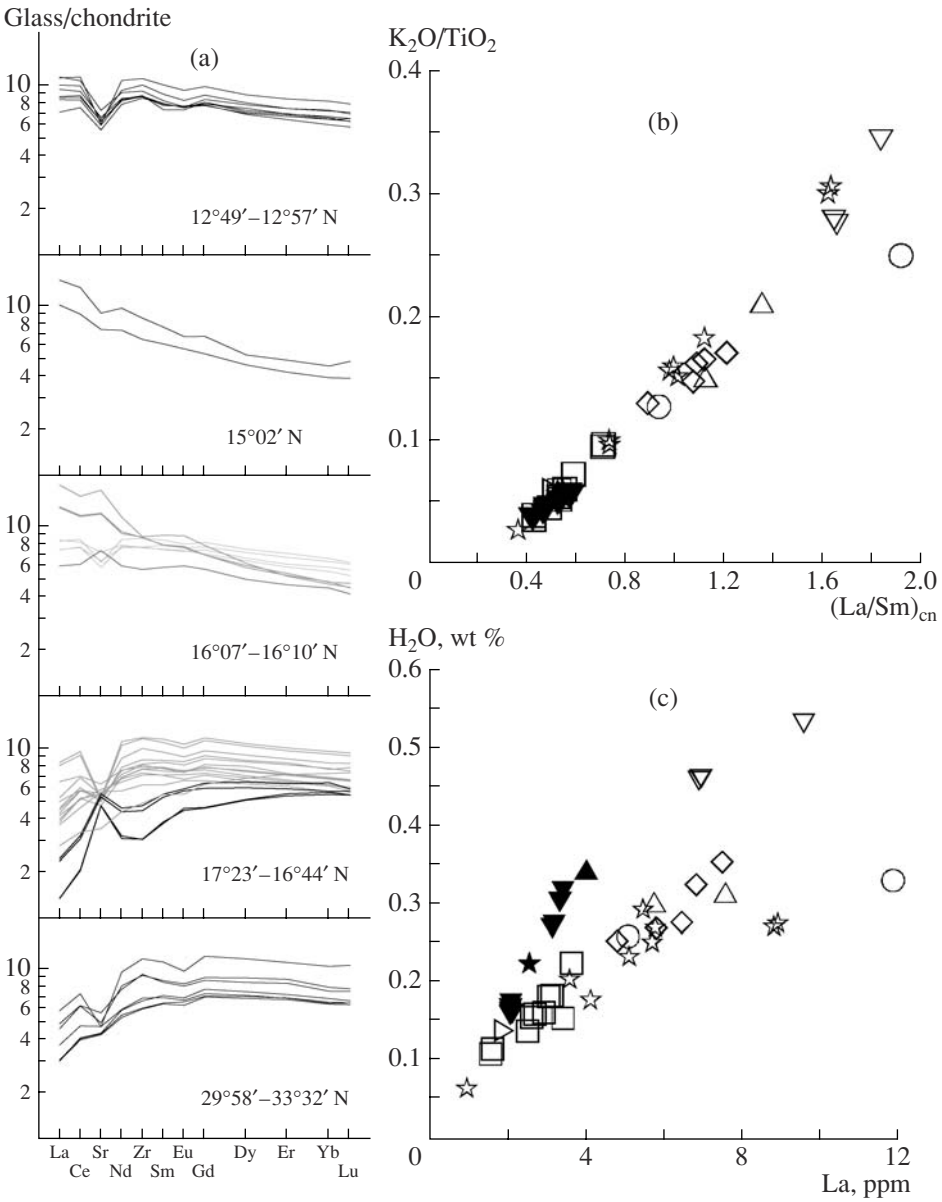

Fig. 5. (a) Distribution of incompatible elements in chilled glasses from various MAR segments between 12°49′ and 17°23′ N and between 29°59′ and 33°41′ N and (b, c) variations in (b) the K_2O/TiO_2 vs. $(La/Sm)_{cn}$ and (c) La vs. H_2O in the same samples. The concentrations were always normalized to CI chondrite (Sun and McDonough, 1989). See Fig. 2 for symbol explanations.

glasses from the MAR segments in question, with this distribution reflecting the specifics of the mantle sources of magmatism at MAR between 29° and 34° N and between 12° and 17° N.

The distribution of incompatible elements in our glasses is generally analogous to that determined previously for the association of depleted and enriched MORB in the vicinity of the Iceland superplume (Chauvel, 2000): the most depleted glasses display positive anomalies of primitive mantle- or CI chondrite-normalized concentrations of Sr and Ba and negative anomalies for Zr and Hf. As in the rocks examined in (Chauvel, 2000), these anomalies in chilled glasses from the two MAR regions become lower with increasing sums of the concentrations of trace elements in these glasses.

The data presented above allow for the occurrence of a small-scale compositional heterogeneity, which is manifested in the distributions of trace elements and REE in chilled glasses across the trend of the rift valley of MAR between 16°06′ and 16°07′ N. It is also reasonable to conclude that the concentration levels of highly incompatible elements (or the degree of enrichment of magmatic products in the rift valley) in the MAR seg-

ments at 15°02′ N and 16°07′ N are comparable with those in the area of a geochemical anomaly at 14°48′ N (Bougault et al., 1988; Dosso et al., 1991; Xia et al., 1992).

Water, Chlorine, and Sulfur

One of the most principally important issues in interpreting data on volatiles in geochemically contrasting MORB series is the identification of the possible source of these elements and the evaluation of the effects of magmatic and hydrothermal processes on the behavior of these elements during the accretion of the oceanic lithosphere.

It was demonstrated in one of the first large publication devoted to the estimation of the behavior and accumulation of water in the suboceanic mantle (Michael, 1998) that glasses enriched in incompatible elements are characterized by higher H_2O concentrations than those in glasses of the N-MORB family. The same author also noted a systematic increase in the H_2O content with decreasing Mg/(Mg + Fe) ratio within each of the examined glass groups and suggested that H_2O behaves as a more compatible element than K, Rb, Nb, and Cl but a less compatible element than Sm, Zr, and Ti during the fractionation of trace elements in the suboceanic upper mantle. Later, Michael (1995) proposed the following succession of incompatibility of elements in magmatic systems generating MORB: La > H_2O ≈ Ce > Nd (i.e., H_2O/La is close to Nd/Ce). Sobolev and Chaussiidon, 1996) published analogous evaluations for the H_2O concentrations in melt inclusions from depleted and enriched MORB.

The results of our research show that low-K spreading basalts (N-MORB) that occur at 29°–34° N, 12.82° N, and 17° N are characterized by high H_2O/K_2O ratios, which indicates that H_2O dominates over K_2O in the magmatic source (Fig. 6a). The products of plume magmatism (13°–15° N and 16° N) are characterized by lower H_2O/K_2O ratios (Fig. 6b, Table 2). Recall that the highest H_2O/K_2O ratio was previously determined also in highly depleted melt inclusions from MAR (Sobolev and Chaussiidon, 1996).

Judging by the H_2O and MgO proportions in the chilled glasses from MAR between 29° and 34° N, the variations in the H_2O contents at MgO variations within a very narrow range reflect local variations in the H_2O contents in the magmatic source of N-MORB in the area. As in (Danyushevsky et al., 2000), these data testify to a strong correlation between the H_2O concentrations in the chilled glasses and other incompatible elements and the $(La/Sm)_{cn}$ parameter. The data presented in Fig. 5b confirm the idea expressed in (Danyushevsky et al., 2000) that H_2O behaves similarly to La in melts generating MORB. It is worth mentioning that the $(La/Sm)_{cn}$ ratio reaches its highest values in plume basalts with the lowest H_2O/K_2O = 0.5–1.5.

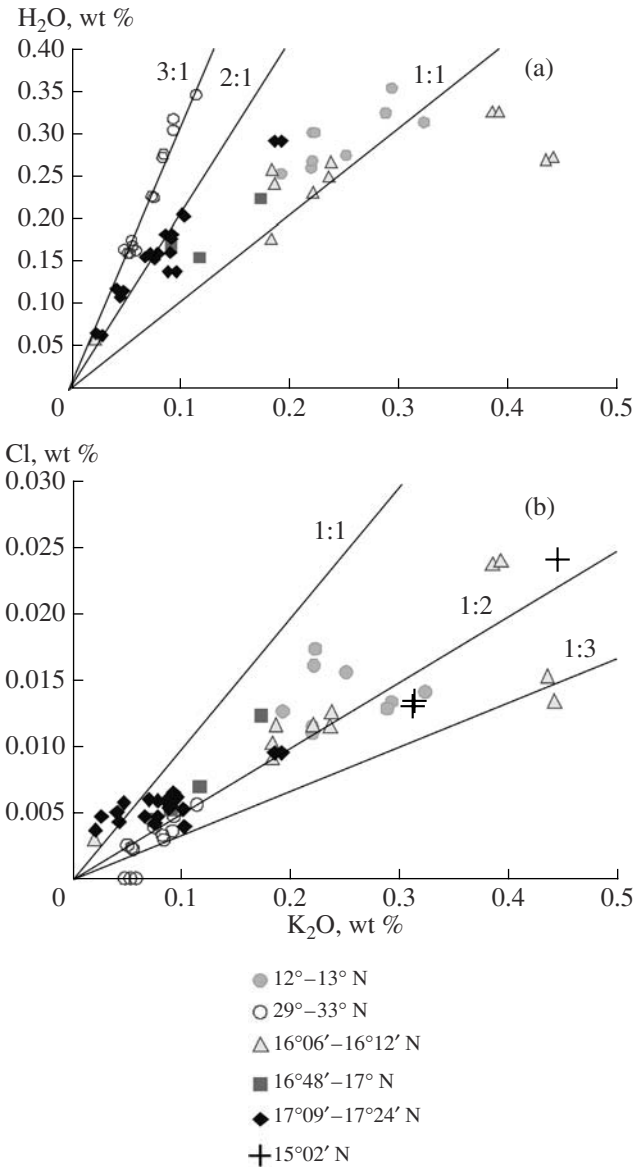

Fig. 6. Correlations between concentrations of (a) H_2O and (b) Cl with the K_2O concentrations in chilled glasses from various MAR segments between 12°49′ and 17°23′ N and between 29°59′ and 33°41′ N.

Michael (1995) examined variations in the contents of H_2O and some trace elements in laterally separated mantle sources of depleted MORB and managed to prove that the H_2O/Ce ratio is constant in N-MORB and E-MORB within each of the areas but significantly varies from region to region. The variations in H_2O/Ce determined in our chilled glasses from MAR are generally consistent with the estimates reported in (Michael, 1995). Glasses from between 29° and 34° N are characterized by a H_2O/Ce ratio corresponding to the range of its values typical of N-MORB and E-MORB from MAR north of 22° N: 240–280 (Fig. 7a). At the same time, the region of 12°–17° N is characterized by extremely broad variations in the H_2O/Ce ratio, corre-

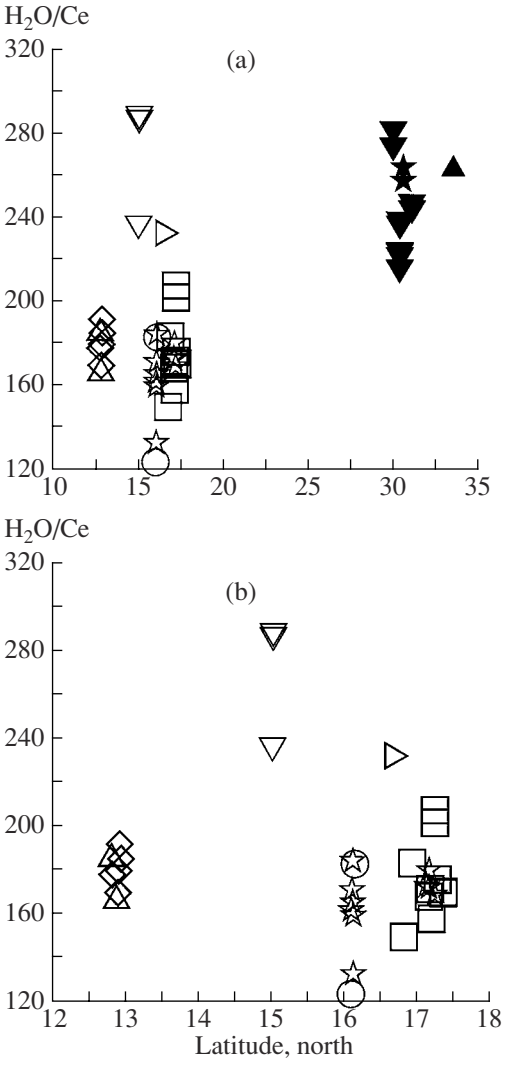

Fig. 7. Variations in the H_2O/Ce ratio in chilled glasses from MAR segments (a) between 12°49′ and 17°23′ N and between 29°59′ and 33°41′ N and (b) between 12°49′ and 17°23′ N. See Fig. 2 for symbol explanations.

sponding to the whole spectrum of ratio reported in (Michael, 1995) for the worldwide MOR system: 155–280 (±50 for each region) (Fig. 7a). Note that the H_2O/Ce ratio principally differs from those of the two aforementioned sharply localized areas of plume magmatism: 15°02′ N and 16°06′ N (Fig. 7b). Inasmuch as the H_2O/Ce ratio shows no correlations with such parameters as the spreading velocity and the degree and depth of melting (Michael, 1995), it is reasonable to believe that this ratio reflects some primary characteristic of the mantle source.

The most comprehensive and updated review of data on Cl concentration in MORB and its correlation with the concentrations of major elements is presented in (Michael and Cornell, 1988), which comprises data on more than 400 samples of basaltic glasses collected in

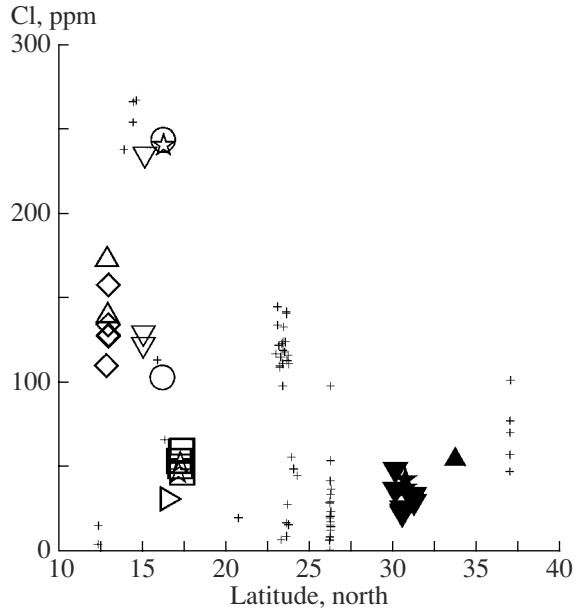

Fig. 8. Variations in the Cl concentration in chilled glasses from MAR segments between 12°49′ and 17°23′ N and between 29°59′ and 33°41′ N. Small crosses correspond to Cl concentrations in MORB glasses from the axial MAR zone reported in (Michael, 1989; Michael and Cornell, 1998). See Fig. 2 for symbol explanations.

20 regions in the ocean. Available data indicate that Cl concentrations in primitive MORB are 20–50 ppm, and these values in the glasses systematically increase with decreasing MgO contents, so that the most fractionated basalts (Fe–Ti MORB) contain approximately 1100 ppm Cl (Michael, 1989; Michael and Cornell, 1998).

The MAR segments examined in the course of our research principally differ by Cl concentrations in their chilled glasses: the MAR axial zone between 29° and 34° N is characterized by notably lower Cl concentrations in glasses than the anomalous MAR segments between 12° and 17° N (Fig. 8). The highest Cl concentrations were found in glasses from the local geochemical anomalies at 15°02′ N and 16°06′ N. Our chilled glasses displayed a negative correlation of the Cl concentrations with the H_2O/K_2O ratio and a positive correlation with the $(La/Sm)_{cn}$ ratio (Fig. 9) and the Sr concentrations. Michael and Cornell (1998) have demonstrated that MORB crystallizing under high pressures have low Cl/K ratios: close to 0.01 for N-MORB and 0.05–0.08 for P-MORB. Our data confirm this conclusion and testify that the highest Cl concentrations are typical of melts that crystallize in the shallowest environments, which is consistent with the aforementioned interpretation of the variations in the Fe_8 value in our collection.

The Cl/K parameter is used in (Michael and Cornell, 1998; Kent et al., 1999) as an indicator of the assimilation of hydrothermally recycled oceanic lithosphere

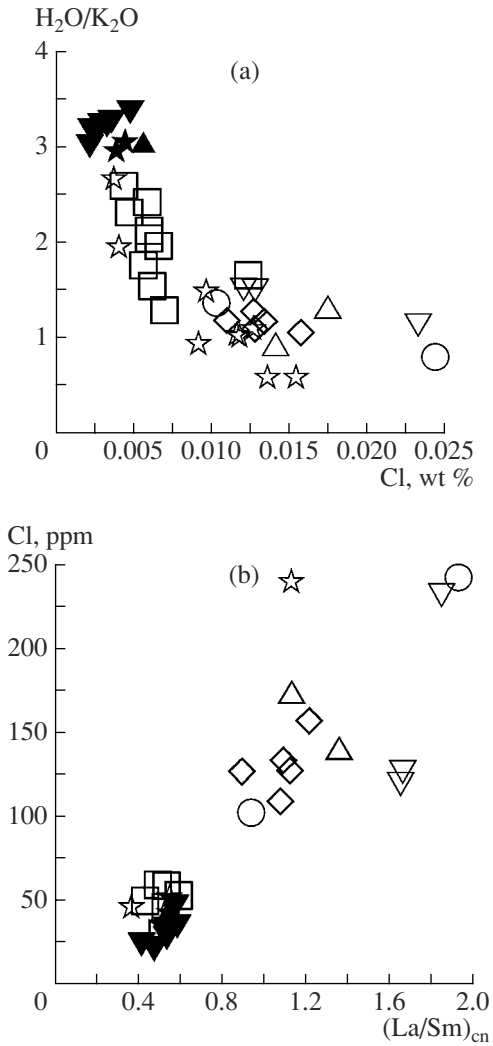

Fig. 9. Variations in the Cl concentration depending on (a) the H_2O/K_2O ratio and (b) the $(La/Sm)_{cn}$ ratio in the chilled glasses. The concentrations were normalized to C1 chondrite (Sun and McDonough, 1989). See Fig. 2 for symbol explanations.

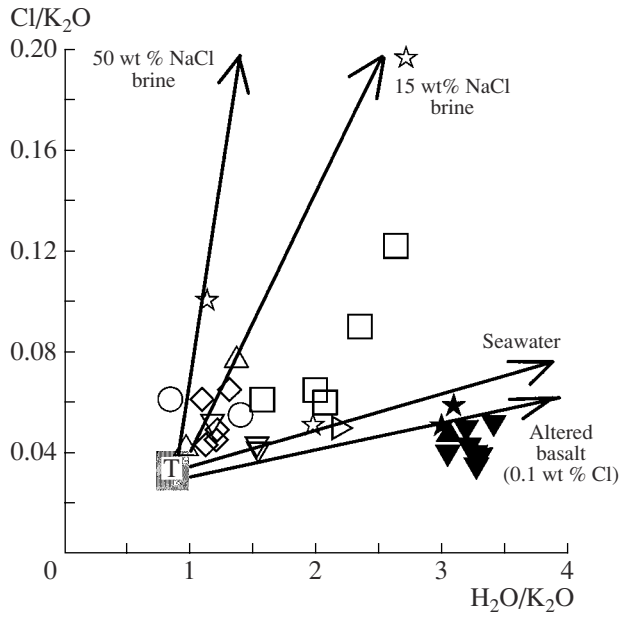

Fig. 10. Arrangement of the data points of the chilled glasses in an H_2O/K_2O vs. Cl/K_2O diagram. The mixing trends, their end members, and the composition of tholeiite (T) are given according (Kent et al., 1999). See Fig. 2 for symbol explanations.

hosting magmatic sources by melts. Applying the approaches used in these papers, it can be assumed that the differences in the variations in the Cl concentrations of glasses from the MAR segments described here reflect the assimilation of various types of crustal contaminants by the melts. For glasses from the MAR segment between 29° and 39° N, this contaminant could be, according to (Kent et al., 1999), the material of low-temperature altered basalts, whereas the melts generating plume MORB should have assimilated oceanic crustal material containing hydrothermal brines that had been formed during the exsolution of hydrothermal solutions at high temperatures (Fig. 10). However, it should be mentioned that the variations in the Cl/K parameter in our glasses may also reflect the differences in the K_2O concentrations (and the H_2O/K_2O ratio) in the parental melts that generated MORB in normal MAR segments between 29° and 34° N and in anomalous segments between 12° and 17° N.

The S concentrations in our samples were obviously directly related to the fractionation of the parental melts, because our samples display a clearly pronounced correlation between S and the Mg# of the rocks (Fig. 11).

The data presented above on the concentrations of volatile components in our collection of chilled glasses testify that the sources of plume magmatism in MAR between 12° and 17° N differ from the source of spreading magmatism at 29°–34° N in the relative H_2O concentration in the magmatic system (the H_2O/K_2O ratio) and, perhaps, also in having much higher Cl concentrations. The isotopic data presented above make it possible to more reliably assay how the geochemical features of the chilled glasses discussed above reflect the primary characteristics of the mantle magmatism sources.

Sr, Nd, AND Pb ISOTOPIC GEOCHEMISTRY

The Sr and Nd isotopic signatures of our samples and the differences between these parameters of rocks from the two axial MAR segments are consistent with the longwavelength geochemical segmentation described in several fundamental publications (Schilling et al., 1983; Hart, 1984; Klein and Langmuir, 1987; Bougault et al., 1988; Dmitriev et al., 1990; Dosso et al., 1991, 1999;

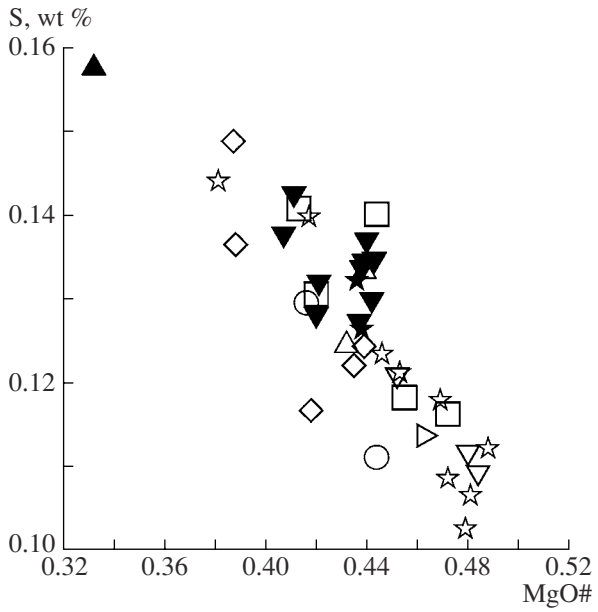

Fig. 11. Variations in the S concentration depending on Mg# = MgO/(MgO + FeO*) in chilled glasses from MAR segments between 12°49′ and 17°23′ N and between 29°59′ and 33°44′ N. See Fig. 2 for symbol explanations.

Taylor et al., 1997). The distribution character of Sr, Nd, and Pb isotopic ratios in MORB along the MAR axis in the northern hemisphere allowed the authors of the aforementioned publications to state that the isotopic segmentation of the MAR axial zone is defined by alternating spreading and plume regions, and the whole spectrum of characteristic isotopic ratios typical of MORB in the Central Atlantic may be accounted for by the mixing of two mantle end members: DM (depleted mantle) and HIMU (enriched mantle with high $^{238}U/^{204}Pb$ ratios). Glasses from the 29°–34° N MAR segments are isotopically analogous to typical N-MORB derived by the melting of DM. The Sr and Nd isotopic composition of chilled glasses collected at the MAR axial zone between 12° and 17° N indicate that this region is characterized by shortwavelength geochemical segmentation with alternating rift valley segments containing N-MORB and sharply localized zones bearing enriched basalts of the P-MORB family (Table 4). The most enriched P-MORB between 12° and 17° N are spatially restricted to localized anomalies at 15°02′ N and 16°07′ N and are characterized by the lowest $^{143}Nd/^{144}Nd$ isotopic ratios (Fig. 12a). The Sr isotopic composition of our glasses suggests the absence of obvious evidence of the low-temperature interaction of most of the rocks with seawater. The exception is one sample, which was taken between 29° and 34° N, and has a Cl concentration and the K_2O/TiO_2 ratio as in other samples from this segment

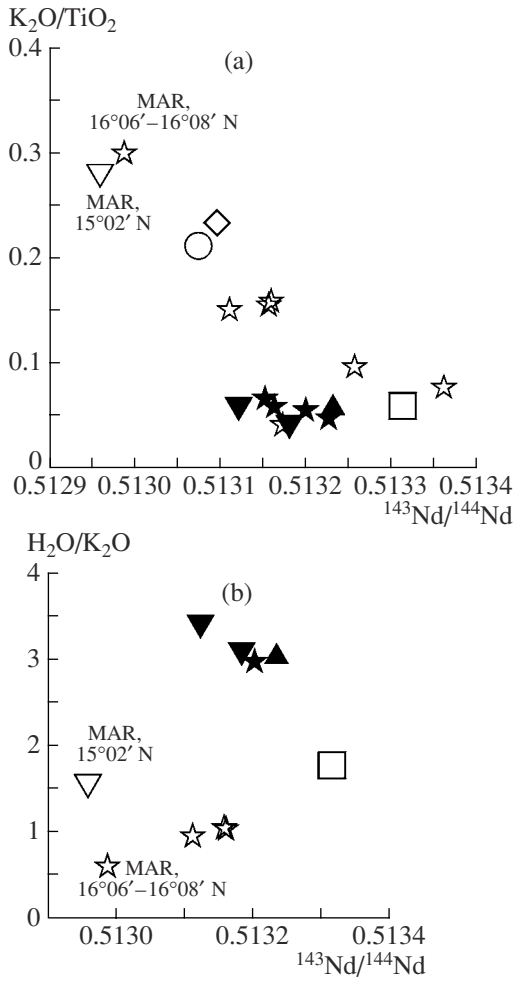

Fig. 12. Variations in the (a) K_2O/TiO_2 and (b) H_2O/K_2O ratios depending on the Nd isotopic composition ($^{143}Nd/^{144}Nd$) in the chilled glasses. See Fig. 2 for symbol explanations.

but an elevated $^{87}Sr/^{86}Sr$ ratio (Fig. 13). It should also be mentioned that this sample is characterized by a high S concentration.

The distribution character of the $^{143}Nd/^{144}Nd$ ratio in samples from our collection display pronounced correlations between the Nd and Sr isotopic compositions and the concentrations levels of volatiles. Samples with high Cl concentrations and low H_2O/K_2O ratios exhibit the lowest $^{143}Nd/^{144}Nd$ ratio (Fig. 12b) and the highest $^{87}Sr/^{86}Sr$ ratio (Fig. 13b). It is worth mentioning that the Cl/K ratio, which reflects, according to (Michael and Cornell, 1998), the degree of assimilation of hydrothermally altered crustal material by the MORB melt, is correlated with the $^{143}Nd/^{144}Nd$ ratio so that the lowest values of this ratio are inherent in the most enriched glasses from the localized plume anomalies at 15°02′ N and 16°07′ N. The lowest S concentrations were detected in samples of the most primitive chilled glasses, which were characterized by a high Mg# and

Table 4. Sr, Nd, and Pb isotopic composition of chilled glasses from the studied MAR segments

Sample no.	$^{87}Sr/^{86}Sr$	$^{143}Nd/^{144}Nd$	$^{206}Pb/^{204}Pb$	$^{207}Pb/^{204}Pb$	$^{208}Pb/^{204}Pb$
16ABP-7-9A/AR1	0.702662	0.513203	n.a.	n.a.	n.a.
16ABP-10	0.702564	0.51323	n.a.	n.a.	n.a.
16ABP-35-7	0.70268	0.513155	n.a.	n.a.	n.a.
16ABP-7-3	0.70268	0.513166	n.a.	n.a.	n.a.
16ABP-24-6	0.703084	0.513235	n.a.	n.a.	n.a.
16ABP-45-77/AR1	0.702688	0.513124	n.a.	n.a.	n.a.
16ABP-6-4/AR2	0.702589	0.513184	n.a.	n.a.	n.a.
16ABP-65-1/AR1	0.70279	0.512961	n.a.	n.a.	n.a.
L20-729-2/GL	0.702175	0.513316	17.5905	15.397	37.002
L20-744-9	0.702453	0.513176	18.036	15.4861	37.619
L20-792-3/GL	0.702737	0.513113	18.5136	15.5201	38.033
L20-793-2/GL	0.702568	0.513162	18.4463	15.5178	37.991
L20-794-2/GL	0.702805	0.512989	18.4204	15.5365	37.909
L20-796-3/GL	0.702576	0.513159	18.4238	15.5053	37.947
L20-733-1	0.702264	0.51326	17.9665	15.4495	37.457
L20-733-13b	n.a.	n.a.	17.9653	15.4533	37.458
L20-738-1	0.702163	0.513364	17.5288	15.3963	36.969
L20-811-2	0.702902	0.513076	18.6904	15.5473	38.301
L20-719-1	0.702268	n.a.	17.5217	15.3937	36.961
L20-773-3	0.702488	0.513204	18.2349	15.4935	37.784
L20-827-2-3	0.702693	0.513098	18.8185	15.5428	38.371

Note: n.a.—means that the isotopic composition was not analyzed.

low $^{143}Nd/^{144}Nd$ ratios. It is reasonable to hypothesize that these correlations suggest lower S concentrations in the mantle sources of magmatism of the localized anomalies at 12°–17° compared with the mantle sources of N-MORB at 29°–34° N.

In the course of this research, we determined Pb isotopic composition only in glasses from the MAR axial zone between 12° and 17° N. The $^{206}Pb/^{204}Pb$ and $^{207}Pb/^{204}Pb$ ratios of the chilled glasses are well correlated with the $^{143}Nd/^{144}Nd$ and $^{87}Sr/^{86}Sr$ ratios for the same samples (Fig. 14). The most enriched glasses with low H_2O/K_2O ratios exhibit the highest $^{206}Pb/^{204}Pb$ ratios. The highly depleted glasses of the N-MORB type from the rift valley between 17°09′ and 17°24′ N show $^{206}Pb/^{204}Pb$ ratios that are likely the lowest among all values for MAR basalts in the northern hemisphere (see, for example, Dosso et al., 1999).

The data presented above on the Sr, Nd, and Pb isotopic composition of chilled glasses from MAR between 29° and 34° N and between 12° and 17° N indicate that the mantle magmatism sources in these rift valley segments show evidence of shortwavelength isotopic heterogeneity. This heterogeneity is most conspicuously pronounced in MAR between 12° and 17° N. The northernmost part of this segment includes a zone with high gradients in the distributions of indicator isotopic–geochemical characteristics of magmatic products in the rift valley. The correlations revealed between the $^{87}Sr/^{86}Sr$, $^{143}Nd/^{144}Nd$, and $^{206}Pb/^{204}Pb$ ratios and the Cl concentrations in our glass samples suggest that the differences in the Cl concentration of glasses from the two MAR segments reflect the primary geochemical specifics of the mantle magmatic sources. This assumption finds further support in a correlation between the Cl

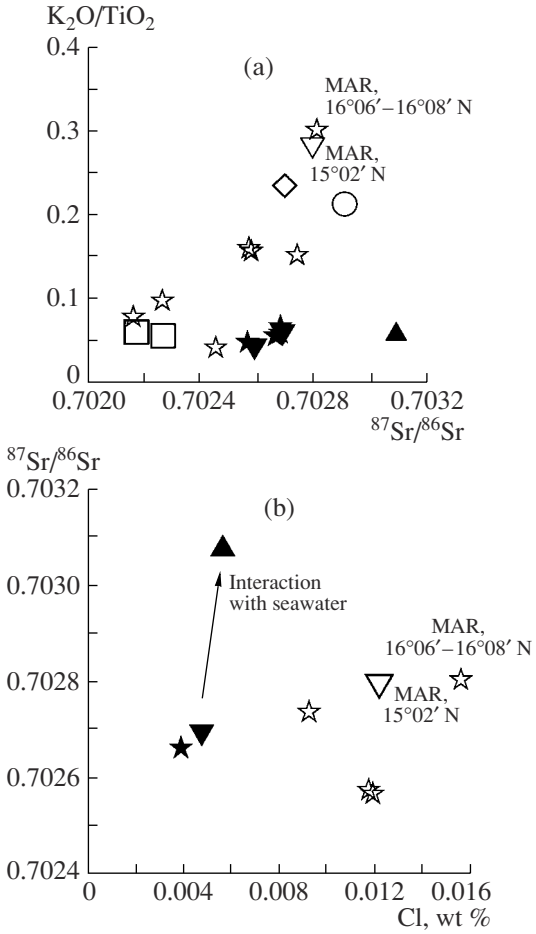

Fig. 13 Variations in the (a) K_2O/TiO_2 ratio and (b) Cl concentration depending on the Sr isotopic composition ($^{87}Sr/^{86}Sr$) in the chilled glasses. The Sr isotopic composition trend for the interaction of the glasses with seawater pertains to sample 16ABP-24-6, which is characterized by the maximum S concentration. See Fig. 2 for symbol explanations.

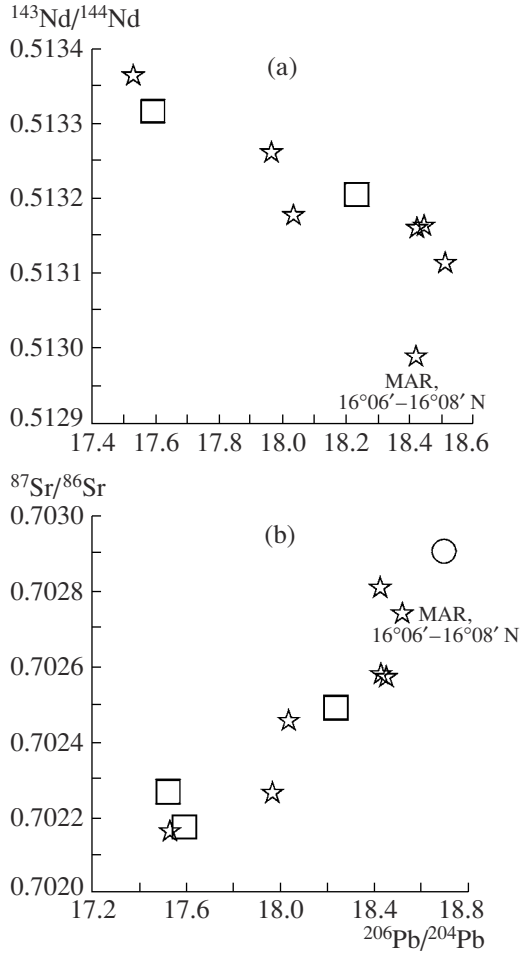

Fig. 14. Variations in the $^{206}Pb/^{204}Pb$ vs. $^{143}Nd/^{144}Nd$ and $^{87}Sr/^{86}Sr$ in chilled glasses from MAR segments between 12°49′ and 17°23′ N and between 29°59′ and 33°41′ N. See Fig. 2 for symbol explanations.

concentrations in the chilled glasses and their K_2O/TiO_2 and H_2O/K_2O ratios.

CONCLUSIONS

The results of our research make it possible to evaluate the composition of the mantle sources of basaltic magmatism in two geodynamically contrasting MAR segments: at 12°–17° N and 29°–34° N. The recently obtained data presented in this publication provide insight into the shortwavelength compositional segmentation in MAR segments that have not studied in this respect.

It was demonstrated above that the differences between the concentrations of major and trace elements and the Sr, Nd, and Pb isotopic composition in chilled glasses from the MAR segments between 29° and 34° N point that the mantle magmatic sources in the corresponding latitudinal interval of the rift valley belonged to the DM type, which is parental for N-MORB. Our data testify that the magmatic sources in the MAR segment between 29° and 34° N have homogeneous distributions of LREE and K_2O but heterogeneous distributions of some strongly incompatible elements. All of our data reported above demonstrate geochemical and isotopic similarities of the chilled glasses from the axial high and the western wall of the rift valley at 17°09′–17°18′ N and 29°–34° N, which led us to ascribe the magmatic products in the rift valley north of 17° N to the N-MORB family. Low-K spreading basalts (N-MORB) at 29°–34° N, 12°49′ N, and north of 17° N are characterized by high H_2O/K_2O ratios, which provide evidence that H_2O dominated over K_2O in the magmatic source. It is also reasonable to think than the magmatic sources of N-MORB at 29°–34° N are locally heterogeneous with respect to H_2O content. The examined MAR segments show basically different Cl concentrations in their chilled glasses: the axial ridge

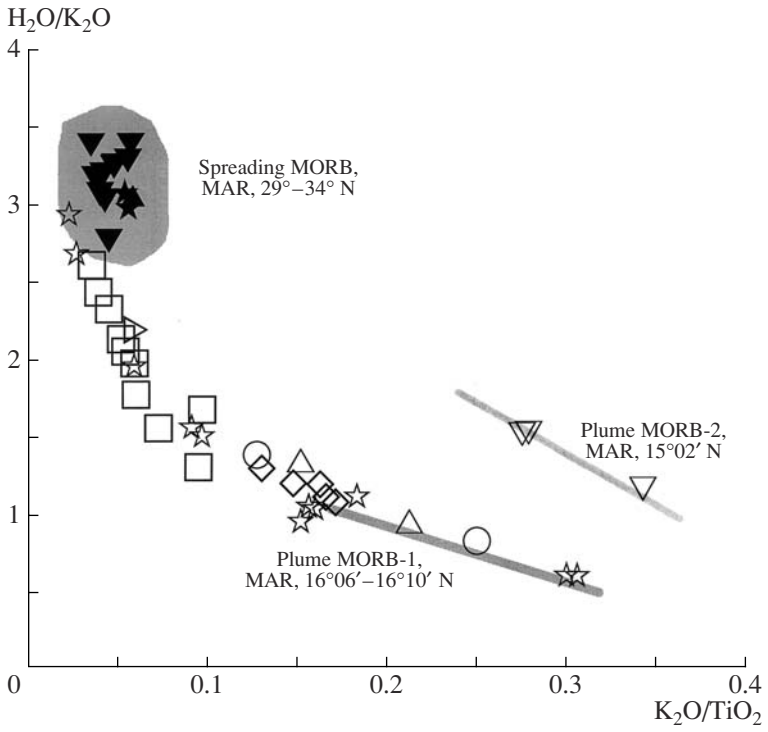

Fig. 15. Variations in the composition of the chilled glasses in a K_2O/TiO_2 vs. H_2O/K_2O distribution and the major geochemical types of basaltic associations in MAR segments between 12°49′ and 17°23′ N and between 29°59′ and 33°41′ N. See Fig. 2 for symbol explanations.

zone between 29° and 34° N is characterized by much lower Cl concentrations in the glasses than the anomalous MAR segments at 12°–17° N. The character of variations in the S concentrations in the glasses demonstrates stronger fractionation of the melts that produced P-MORB at 12°–17° N compared to the melts that gave rise to N-MORB in the MAR axial zones between 29° and 34° N, which may reflect the effect of a low-temperature hydrothermal process on the rocks, which is also pronounced in the Sr isotopic composition of the sample.

Signatures of plume magmatism are clearly pronounced within a long MAR interval between 12° and 17° N, which includes two sharply localized zones of plume magmatism at 15°02′ N and 16°07′ N. These localized zones display the lowest degrees of melting in the magmatic sources. Judging from our data, the most enriched basaltic glasses from the area correspond to the lowest pressures of cotectic crystallization. Evidently, the parental melts of P-MORB in these localized areas ascended to the surface from shallow magmatic chambers. This idea is consistent with the model for the genesis of enriched MORB in the Central Atlantic (Halliday et al., 1995), which assumes the existence of near-surface fractionated (NSF) sources beneath the axial zone of the ridge, which are characterized by high $^{206}Pb/^{204}Pb$ ratios, i.e., having isotopic–geochemical signatures close to HIMU. The products of plume magmatism at 12°–17° N are generally characterized by lower H_2O/K_2O ratios that those of N-MORB from 29°–34° N but much higher Cl concentrations. These geochemical features are most conspicuous in the localized plume sources at 15°02′ and 16°07′ N.

The MAR segment between 12° and 17° N is characterized by shortwavelength compositional segmentation along its axis and local geochemical heterogeneity, which is manifested in the concentrations of trace elements and REE in the chilled glasses across the trends of some segments of the MAR rift valley. It has been demonstrated (Dosso et al., 1991) that the rift valley of MAR north of the 15°02′ transform fault contains basalts geochemically belonging to N-MORB, and their degree of enrichment increases from north to south. This geochemical phenomenon was interpreted (Dosso et al., 1991) as reflecting the influence of an anomalous mantle magmatic source situated in the area of 14° N. At the same time, Sobolev et al. (1992) reported data testifying to the existence of another (northern) maximum in the degree of enrichment of the basalts in incompatible elements, which coincides with the southern boundary of the transform fault (15°10′–15°15′ N). Isotopic–geochemical data presented above suggest that plume magmatism is widespread north of the 15°02′ transform fault, within the northern MAR segment, which was previously thought to be an area of exclusively spreading magmatism. It should be added that the level of the concentrations of strongly incompatible elements in the sharply localized geochemical

anomaly discovered in the course of our research at 16°07′ N is comparable with that at the geochemical anomaly at 14°48′ N. The anomaly at 16°07′ N is likely also reflected in the surface topography of the seafloor, which shows there an axial high in the rift valley (Le Douaran and Francheteau, 1981).

As was mentioned above, the chilled glasses from the localized plume anomalies at 15°02′ N and 16°07′ N display geochemical differences in such indicator parameters as the H_2O/K_2O and H_2O/Ce ratios. These differences can likely reflect the participation of two mantle sources of plume magmatism in the genesis of P-MORB in these MAR segments, with these sources characterized by different H_2O concentrations. The possibility of the participation of two mantle source in MAR magmatism between 12° and 17° N is illustrated in Fig. 15, which exhibits the variations in the H_2O/K_2O and K_2O/TiO_2 ratios in our collection of chilled glasses. The diagram shown in Fig. 15 suggests the occurrence of three major magmatic MORB series in the Central Atlantic: (1) spreading (29°–34° N); (2) transitional from spreading to plume, with isotopic–geochemical signatures of the interaction of two compositionally contrasting magmatic sources (12°–17° N), which corresponds to T-MORB; and (3) plume proper (15°02′ N and 16°07′ N). This conclusion is consistent with the currently adopted systematics of MORB, according to which the whole diversity of the geochemical types of MOR basalts can be described in N-MORB vs. T-MORB vs. P-MORB space.

It is reasonable to suggest that melts were generated in the MAR segment between 29° and 34° N from depleted mantle sources like DM with a homogeneously distributed K_2O/TiO_2 ratio, in a geodynamic environment typical of normal MAR segments. MAR segments between 12° and 17° N combine contrasting geodynamic environments of their magmatism that determined the development of a large plume region with widespread mixing of the melting products of geochemically distinct mantle sources. At the same time, this region was characterized by conditions favorable for the origin of sharply localized zones of anomalous magmatism of the plume type. These sporadic magma sources are spatially restricted to MAR segments with Hess crust (with the predominance of mantle peridotites), whose mechanical and compositional characteristics may facilitate the focusing and localization of plume magmatism.

Thus, one of the most principal geochemical parameters in the discrimination of mantle magmatic sources that generate N-MORB and P-MORB in MAR in the northern hemisphere may be the H_2O/K_2O ratio. Low values of this ratio in true MORB, whose $^{206}Pb/^{204}Pb$ ratios are the closest to those of mantle sources with HIMU signatures, are determined by high K_2O concentrations in the magmatic source. The data presented above provide evidence of variations in the Cl concentrations and the Cl/K ratio in the chilled glasses of N-MORB and P-MORB. Persistent correlations between these parameters and isotopic–geochemical indicators of the nature of mantle sources parental for the glasses provide sound grounds to believe that the variations in the Cl concentrations and Cl/K ratio in these glasses most probably reflect the geochemical specifics of the mantle magmatic sources but not a result of assimilation of altered crustal material. With regard for data on and considerations of Cl behavior in the magmatic system of MOR presented in (Michael and Cornell, 1998), an alternative explanation can be proposed for this fact based on the assimilation of the material of ancient recycled oceanic lithosphere by the parental melts. However, in such interpretation of the Cl distribution in MORB chilled glasses, it should also be concluded that the Cl concentrations in the crustal contaminant in the plume segments of the MAR axial zone (particularly, in the sharply localized segments) should be higher than in the contaminated material of normal MAR segments.

The comparison of the results obtained in our research with currently available information on the geochemical segmentation of MAR allowed us to hope that the MAR segment immediately north of 16° N is highly promising for searches for new hydrothermal fields. The high-gradient geochemical anomaly discovered in this MAR segment and the wide occurrence of mantle residues in it are mandatory attributes of hydrothermal fields recently found south of the 15°02′ transform fault zone.

ACKNOWLEDGMENTS

The authors thank L.V. Dmitriev, T. Faloon, J. Bedard, and P. Michael for fruitful discussions of various aspects of magmatism in mid-oceanic ridges. Our research was greatly facilitated by the use of basaltic glass standards provided for us the Museum of Natural History, Washington, D.C. This study was financially supported by the Russian Foundation for Basic Research (project no. 03-05-64018 and 06-05-64003) and the joint Russian–French project “The Mid-Atlantic Ridge Geodynamics and the Ore Formation Processes”.

REFERENCES

1. D. Bideau, R. Hekinian, B. Sichler, et al., “Contrasting Volcanic–Tectonic Processes during Past 2 Ma on the Mid-Atlantic Ridge: Submersible Mapping, Petrological and Magnetic Results at Lat. 34°52′N and 33°55′N,” Marine Geophys. Res. **20**, 425–458 (1998).
2. H. Bougault, L. Dmitriev, J.-C. Schilling, et al. “Mantle Heterogeneity from Trace Elements: MAR Triple Junction near 14°N,” Earth Planet. Sci. Lett. **88**, 27–36 (1988).
3. A. Büchl, C. Münker, K. Mezger, and A. W. Hofmann, “High-Precision Nb/Ta and Zr/Hf Ratios in Global MORB,” Geochim. Cosmochim. Acta. Spec. Suppl. **66**, A108 (2002).

4. M. Cannat and J. F. Casey, "An Ultramafic Lift at the Mid-Atlantic Ridge: Successive Stages of Magmatism in Serpentinized Peridotites from the 15°N Region," in *Mantle and Lower Crust Exposed in Oceanic Ridges and in Ophiolites*, Ed. by R. L. M. Vissers and A. Nicolas. (Kluwer, Norwell–Dordrecht, 1995), pp. 5–34.
5. J. F. Casey, W. B. Bryan, and S. Silantyev, "Major and Trace Element Geochemistry of Basalts, Gabbros and Peridotites from the Northern MAR: An Assessment of the Range of Subaxial Parental and Evolved Melt Compositions," in *AGU Fall Meeting, San Francisco, USA, 1995* (San Francisco, 1995), p. 694.
6. C. Chauvel, "Melting of a Complete Section of Recycled Oceanic Crust: Trace Element and Pb Isotopic Evidence from Iceland," Geochem. Geophys. Geosyst. **1**, 1999G000003 (2000).
7. L. V. Danyushevsky, A. V. Sobolev, and L. V. Dmitriev, "Estimation of Pressure of Crystallization and H_2O Content of MORB and BABB Glasses: Calibration of an Empirical Technique," Mineral. Petrol. **57**, 185–204 (1996).
8. L. V. Danyushevsky, S. M. Eggins, T. J. Falloon, and D. M. Christe, "H_2O Geochemistry in Depleted to Moderately Enriched Mid-Ocean Ridge Magmas; Part 1: Incompatible Behaviour, Implications for Mantle Storage, and Origin of Regional Variations," J. Petrol. **41**, 1329–1364 (2000).
9. L. V. Dmitriev, W. G. Melson, and M. G. Reisner, "The Distribution of Petrochemical Types of the Tholeiitic Abyssal Glasses," in *International Geological-Geophysical Atlas of the Atlantic Ocean* (IOC, UNESCO, 1990), p. 110.
10. L. Dosso, B. B. Hanan, H. Bougault, et al., "Sr–Nd–Pb Geochemical Morphology Between 10° and 17°N on the Mid-Atlantic Ridge: A New MORB Isotope Signature," Earth Planet. Sci. Lett. **106**, 29–43 (1991).
11. L. Dosso, H. Bougault, C. Langmuir, et al., "The Age and Distribution of Mantle Heterogeneity Along the Mid-Atlantic Ridge (31°–41°N)," Earth Planet. Sci. Lett. **170**, 269–286 (1999).
12. E. Gracia, L. M. Parson, D. Bideau, and R. Hekinian, "Volcano-Tectonic Variability along Segments of the Mid-Atlantic Ridge Between Azores Platform and Hayes Fracture Zone: Evidence from Submersible and High-Resolution Sidescan Sonar Data," in *Modern Ocean Floor Processes and the Geological Record*, Ed. by R. A. Mills and K. Harrison, Geol. Soc. London, Spec. Publ. **148**, 1–15 (1998).
13. A. N. Halliday, L. Der-Chuen, S. Tommasini, et. al., "Incompatible Trace Elements in OIB and MORB and Source Enrichment in the Sub-Oceanic Mantle," Earth Planet. Sci. Lett. **133**, 379–395 (1995).
14. S. R. Hart, "The DUPAL Anomaly: a Large-Scale Isotopic Anomaly in the Southern Hemisphere," Nature **309**, 753–756 (1984).
15. E. Jarosewich, J. A. Nelen, and J. A. Norberg, "Reference Samples for Electron Microprobe Analysis," Geostand. Newslett. **4**, 43–47 (1980).
16. A. J. R. Kent, M. D. Norman, I. D. Hutcheon, and E. M. Stolper, "Assimilation of Seawater-Derived Components in an Oceanic Volcano: Evidence from Matrix Glasses and Glass Inclusions from Loihi Seamount, Hawaii," Chem. Geol. **156**, 299–319 (1999).
17. E. M. Klein and C. H. Langmuir, "Global Correlations of Ocean Ridge Basalt Chemistry with Axial Depth and Crustal Thickness," J. Geophys. Res. **92**, 8089–8115 (1987).
18. S. E. Le Douaran and J. Francheteau, "Axial Depth Anomalies from 10° To 50° North along the Mid-Atlantic Ridge: Correlation with Other Mantle Properties," Earth Planet. Sci. Lett. **54**, 29–47 (1981).
19. P. J. Michael and J.-G. Schilling, "Chlorine in Mid-Ocean Ridge Magmas: Evidence for Assimilation of Seawater-Influenced Components," Geochim. Cosmochim. Acta **53**, 3131–3143 (1989).
20. P. J. Michael and W. C. Cornell, "Influence of Spreading Rate and Magma Supply on Crystallization and Assimilation beneath Mid-Ocean Ridges: Evidence from Chlorine and Major Element Chemistry of Mid-Ocean Ridge Basalt," J. Geophys. Res. **103** (B8), 356 (1998).
21. P. Michael, "Regionally Distinctive Sources of Depleted MORB: Evidence from Trace Elements and H_2O," Earth Planet. Sci. Lett. **131**, 301–320 (1995).
22. P. J. Michael, "The Concentration, Behavior and Storage of H_2O in the Suboceanic Upper Mantle: Implications for Mantle Metasomatism," Geochim. Cosmochim. Acta **52**, 555–566 (1988).
23. Y. Niu and R. Bariza, "Trace Element Evidence from Seamounts for Recycled Oceanic Crust in the Eastern Pacific Mantle," Earth Planet. Sci. Lett. **148**, 471–483 (1997).
24. *RIDGE Petrological Data Baseline* (LGEO, Lamont-Doherty Observatory, New York, 1999).
25. *Relief of the Surface of the Earth. Computer-Generated Coler-Coded Shaded Relief Map*, Ed. by J. R. Hertzler. WHOI., Word Data Center for Marine Geology and Geophysics, Report MGG-2, Sheet-2, 1991.
26. J.-G. Schilling, M. Zajac, R. Evans, et al., "Petrologic and Geochemical Variations along the Mid-Atlantic Ridge from 27°N and 73°N," Am. J. Sci. **283**, 510–586 (1983).
27. *Shipboard Scientific Party. 2003. Leg 209 Preliminary Report*, ODP Prelim. Rpt. **109** [Online].
28. S. A. Silantyev, "Variations in the Geochemical and Isotopic Characteristics of Residual Peridotites along the Mid-Atlantic Ridge as a Function of the Nature of the Mantle Magmatic Sources," Petrologiya **11**, 339–362 (2003) [Petrology **11**, 305–326 (2003)].
29. S. A. Silantyev, B. V. Belyatsky, V. E. Beltenev, et al., "The Distribution of Isotope Signatures in MAR Peridotites Between 12° and 36°N and Two Main Kinds of Mantle Substratum below Ridge Axis," InterRidge News **10** (2), 27–33 (2001).
30. S. A. Silantyev, J. F. Casey, H. J. B. Dick, et al., "How Many Mantle Sources Are Involved in Formation of Residual Peridotites from MAR Between 14° N and 16° N?," Europ. Geophys. Soc. Annales Geophysicae Pt. 1. Soc. Symp. Solid Earth Geophys. Geodesy Suppl. 1 **16**, 294 (1998).
31. S. E. Smith, J. F. Casey, W. B. Bryan, et al., "Geochemistry of Basalts from the Hayes Transform Region of the Mid-Atlantic Ridge," J. Geophys. Res. **103** (B3), 5305 (1998).

32. *Smitsonian Volcanic Glass Data File*, 2000. http://www.nmnh.si.edu/minsci/research/glass/index.htm

33.A. V. Sobolev and M. Chaussidon, "H_2O Concentrations in Primary Melts from Supra-Subduction Zones and Mid-Ocean Ridges: Implications for H_2O Storage and Recycling in the Mantle," Earth Planet. Sci. Lett. **137**, 45–55 (1996).

34.A. V. Sobolev, L. V. Dmitriev, O. P. Tsameryan, et al., "On the Structure and Origin of Geochemical Anomaly in the Second-Layer Basalts between 12 and 18° N of the Mid-Atlantic Ridge," Dokl. Akad. Nauk **326** (3), 541–546 (1992).

35.S.-S. Sun and W. F. McDonough, "Chemical and Isotopic Systematics of Oceanic Basalts: Implications for Mantle Composition and Processes," in *Magmatism in Ocean Basins*, Ed. by A. D. Saunders and M. J. Norry, Geol. Soc. London Spec. Publ. **42**, pp. 313–345 (1989).

36.R. N. Taylor, M. F. Thirlwall, B. Murton, et al., "Isotopic Constraints on the Influence of the Icelandic Plume," Earth Planet. Sci. Lett. **148**, E1–E8 (1997).

37.M. Wilson, *Igneous Petrogenesis* (Unwin Hyman, London, 1989).

38.C. Xia, J. F. Casey, S. Silantyev, et al., "Geochemical Variations between 12 to 16° N, Mid-Atlantic Ridge: A Region with High Degrees of Partial Melting yet Magma Starved?," EOS Trans., Amer. Geophys. Union**73** (43), 553 (1992).